Acta Pharmaceutica Sinica B 2023;13(1):390–409

Chinese Pharmaceutical Association
Institute of Materia Medica, Chinese Academy of Medical Sciences

Acta Pharmaceutica Sinica B

www.elsevier.com/locate/apsb
www.sciencedirect.com

ORIGINAL ARTICLE

Pathologically triggered *in situ* aggregation of nanoparticles for inflammation-targeting amplification and therapeutic potentiation

Qiang Nie[a,†], Chenwen Li[a,†], Yu Wang[b,†], Yi Hu[a], Wendan Pu[a], Qixiong Zhang[a], Jiajun Cai[a], Yongyao Lin[a], Gang Li[a], Chenping Wang[a], Lanlan Li[a], Yin Dou[a], Jianxiang Zhang[a,c,*]

[a]*Department of Pharmaceutics, College of Pharmacy, Third Military Medical University (Army Medical University), Chongqing 400038, China*
[b]*Department of Radiology, Chongqing University Cancer Hospital & Chongqing Cancer Institute & Chongqing Cancer Hospital, Chongqing 400030, China*
[c]*State Key Lab of Trauma, Burn and Combined Injury, Institute of Combined Injury, Third Military Medical University (Army Medical University), Chongqing 400038, China*

Received 3 February 2022; received in revised form 24 April 2022; accepted 28 April 2022

KEY WORDS

Inflammatory disease;
Reactive oxygen species;
Myeloperoxidase;
Targeted therapy;
Nanoparticles;
Surface engineering;
Triggerable aggregation;
Nanotherapy

Abstract Uncontrolled and persistent inflammation is closely related to numerous acute and chronic diseases. However, effective targeting delivery systems remain to be developed for precision therapy of inflammatory diseases. Herein we report a novel strategy for engineering inflammation-accumulation nanoparticles *via* phenolic functionalization. Different phenol-functionalized nanoparticles were first developed, which can undergo *in situ* aggregation upon triggering by the inflammatory/oxidative microenvironment. Phenolic compound-decorated poly (lactide-*co*-glycolide) nanoparticles, in particular tyramine (Tyr)-coated nanoparticles, showed significantly enhanced accumulation at inflammatory sites in mouse models of colitis, acute liver injury, and acute lung injury, mainly resulting from *in situ* cross-linking and tissue anchoring of nanoparticles triggered by local myeloperoxidase and reactive oxygen species. By combining a cyclodextrin-derived bioactive material with Tyr decoration, a multifunctional nanotherapy (TTN) was further developed, which displayed enhanced cellular uptake, anti-inflammatory activities, and inflammatory tissue accumulation, thereby affording amplified therapeutic effects in mice with colitis or acute liver injury. Moreover, TTN can serve as a bioactive and inflammation-targeting nanoplatform for site-specifically delivering a therapeutic peptide to the inflamed

*Corresponding author. Tel.: +86 23 68771637.
E-mail address: jxzhang@tmmu.edu.cn (Jianxiang Zhang).
[†]These authors made equal contributions to this work.
Peer review under the responsibility of Chinese Pharmaceutical Association and Institute of Materia Medica, Chinese Academy of Medical Sciences.

https://doi.org/10.1016/j.apsb.2022.07.013

colon post oral administration, leading to considerably potentiated *in vivo* efficacies. Preliminary studies also revealed good safety of orally delivered TTN. Consequently, Tyr-based functionalization is promising for inflammation targeting amplification and therapeutic potentiation of nanotherapies.

1. Introduction

Inflammation is a basic pathological process and a protective immune response that occurs when tissues and cells are stimulated by harmful endogenous and exogenous irritants, such as pathogens, damaged cells, and chemical/physical injury[1−3]. However, uncontrolled and excessive inflammation is intimately associated with many acute and chronic disorders or diseases[4,5], including acute liver/lung injury[6,7], obesity[8], diabetes[9], non-alcoholic fatty liver disease[10], cardiovascular disease[11,12], inflammatory bowel disease (IBD)[13], and neurodegenerative diseases[14]. For the treatment of inflammatory diseases, different types of therapeutics, such as corticosteroids, nonsteroidal anti-inflammatory drugs (NSAIDs), antioxidants, as well as monoclonal antibodies to various inflammatory cytokines and chemokines are generally used in the clinic[15−17]. Unfortunately, osteoporosis, liver/kidney injury, and gastrointestinal/cardiovascular complications are frequently observed severe side effects resulting from glucocorticoids and NSAIDs[18−21]. As for biological therapeutics, their clinical applications have also been compromised due to low stability and bioavailability, high cost, primary/secondary non-responses, and the increased risk of infections or malignancies[4,22,23]. Regardless of small molecular agents and biological therapies against inflammatory diseases, their systemic exposure or non-specific biodistribution post oral or parenteral administration is a key issue responsible for their adverse drug reactions[24−26]. Therefore, both new drugs and creative delivery strategies are necessary to achieve more desirable treatment of inflammatory diseases.

Site-specific delivery of therapeutic agents to diseased sites is one of the most effective and promising approaches to overcome dose-limiting or drug-related toxicities and enhance *in vivo* efficacies. Increasing evidence has demonstrated that the nanoparticle-based targeting strategy is promising for the treatment of IBD[27,28], atherosclerosis[29−31], asthma[32,33], and other inflammatory diseases[34−37]. Due to the increased vascular permeability at inflammatory sites, different types of nanocarriers, such as liposomes[38], polymeric nanoparticles[39], and inorganic nanomaterials[40], have been examined for suppressing inflammation *via* passive targeting. Taking advantages of overexpressed specific receptors and/or antigens on epithelial/endothelial cells of inflamed tissues, corresponding molecular ligands and/or antibodies are frequently utilized to decorate different nanoplatforms to achieve active targeting, thereby enhancing therapeutic effects[24,39,41−43]. In addition, components of inflammatory/immune cells were employed to coat nanoparticles[44−49], in view of their inflammatory tissue homing capability. Similarly, different microorganisms and eukaryotic cells were used as biomimetic delivery vehicles for inflammation targeting *via* a hitchhiking mechanism[50−54]. Besides inflammation targeting mediated by functional molecules and cellular components, nanoparticles or microparticles derived from bioresponsive materials have been examined for site-specific delivery of diverse therapeutics to inflamed tissues[26,31,55], taking advantage of local acidification, overproduction of reactive oxygen species (ROS), and up-regulated enzymes in the inflammatory microenvironment. Despite these considerable advances in inflammation targeting delivery systems, some crucial challenges remain to be resolved for their clinical translation. For molecular targeting systems, their targeting efficiency need to be further improved, while desirable quality control, cost-efficient mass production, and good reproducibility should be circumvented for different biomimetic vehicles. As for existing inflammation-responsive carriers, their major advantage lies in triggerable release of therapeutic payload.

As well documented, phenolic groups can be oxidized in the presence of peroxidases (such as horseradish peroxidase and myeloperoxidase) and hydrogen peroxide (H_2O_2) to generate free radicals, which further dimerize or yield oligomers[56,57]. This enzyme/H_2O_2-mediated polymerization of phenolic moieties has been employed for enzyme-specific activation of contrast agents for peroxidase imaging in cardiovascular and cerebrovascular diseases[58−61]. Moreover, ROS and myeloperoxidase (MPO) are generally overexpressed in tissues with inflammation and oxidative stress[62−64]. Inspired by these findings and to overcome the above mentioned issues, herein we hypothesize that surface engineering of nanotherapies with phenolic moieties can enhance their targeting capability to inflammatory and oxidative tissue injury sites by ROS/MPO-triggered *in situ* aggregation and enhanced tissue binding, thereby affording improved therapeutic effects (Fig. 1A). As a proof of concept, poly (lactide-*co*-glycolide) (PLGA) nanoparticles were first engineered to screen the most effective phenolic moiety for inflammation-triggered *in situ* clustering and targeting, based on *in vitro* tests and *in vivo* evaluations in different animal models of inflammation and oxidative tissue injury. Further, intrinsically anti-inflammatory nanoparticles and their peptide-containing nanotherapies were investigated to demonstrate the effectiveness of this phenolic functionalization-mediated inflammation-targeting strategy in mouse models of IBD and acute liver injury.

2. Materials and methods

2.1. Materials

1,2-Distearoyl-*sn*-glycero-3-phosphoethanolamine-*N*-[methoxy-(polyethylene glycol)-2000] (DSPE-PEG) and 1,2-distearoyl-*sn*-glycero-3-phosphoethanolamine-*N*-[hydroxysuccinimide (polyethylene glycol)-2000] (DSPE-PEG-NHS) were purchased from Xi'an Ruixi Biological Technology Co., Ltd. (Xi'an, China). Triethylamine (TEA) was obtained from J&K Scientific (Beijing, China). Tyramine (Tyr), serotonin hydrochloride (Ser·HCl), *β*-

cyclodextrin (β-CD), and lecithin (from soybean) were purchased from Tokyo Chemical Industry Co., Ltd. (Tokyo, Japan). Dopamine hydrochloride (Dopa·HCl), 4-hydroxy-2,2,6,6-tetramethylpiperidin-1-oxyl (Tempol), 1,1-carbonyldiimidazole (CDI), 4-(hydroxymethyl) phenylboronic acid pinacol ester (PBAP), and poly (lactide-*co*-glycolide) (PLGA, 75:25) were provided by Sigma−Aldrich (USA). Cyanine5 NHS ester (Cy5) and Cyanine7.5 NHS ester (Cy7.5) were obtained from Lumiprobe, LLC. (USA). APC-CD11b and PE-Ly6G antibodies were from BD Biosciences. FITC-F4/80 antibody was obtained from Biolegend. The peptide Ac2-26 was synthesized by ChinaPeptides Co., Ltd. (Shanghai, China). Dextran sulfate sodium (DSS) (36,000−50,000 Da) was purchased from MP Biomedicals, LLC. (USA). 4′,6-Diamidino-2-phenylindole (DAPI) staining solution was provided by Beyotime Biotechnology (Shanghai, China). 4-Acetamidophenol (APAP) was obtained from Aladdin (Shanghai, China). Myeloperoxidase (MPO) and monocyte chemotactic protein-1 (MCP-1) were purchased from R&D

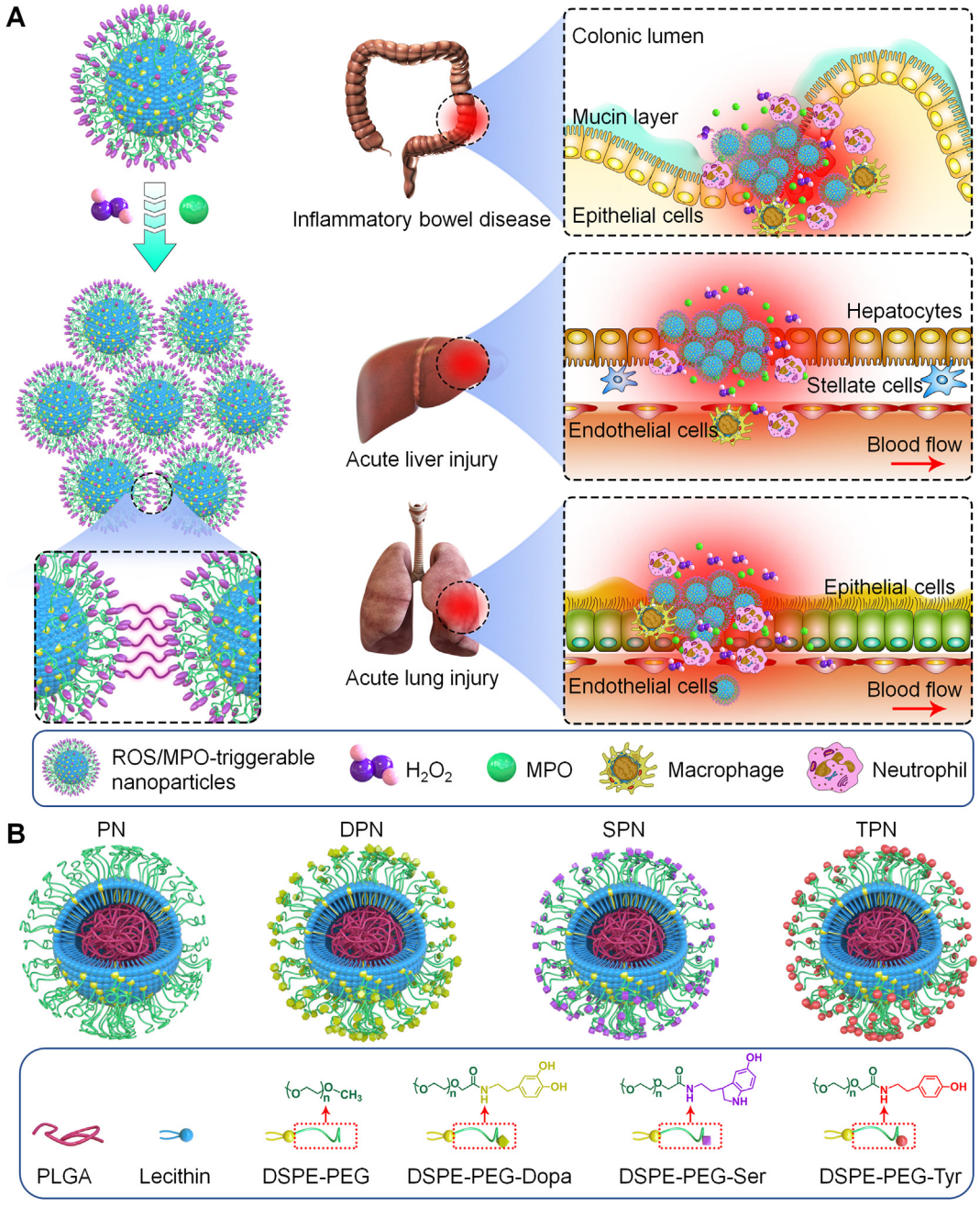

Figure 1 Schematic illustration of ROS/MPO-triggerable nanoparticles for enhanced accumulation at inflammatory and oxidative injury sites by *in situ* aggregation. (A) A sketch showing mechanisms underlying the enhanced accumulation of surface-functionalized nanoparticles for targeted treatment of inflammatory diseases. (B) Engineered PLGA nanoparticles with various surface chemistries. PN, PLGA/DSPE-PEG nanoparticles; DPN, PLGA/DSPE-PEG-Dopa nanoparticles; SPN, PLGA/DSPE-PEG-Ser nanoparticles; TPN, PLGA/DSPE-PEG-Tyr nanoparticles.

Systems Inc. (Minneapolis, MN, USA). Lipopolysaccharides (LPS, O26:B6) and phorbol 12-myristate 13-acetate (PMA) were obtained from Sigma−Aldrich (USA).

2.2. Synthesis and characterization of different materials

DSPE-PEG conjugates based on dopamine (Dopa), serotonin (Ser), or tyramine (Tyr) were defined as DSPE-PEG-Dopa, DSPE-PEG-Ser, and DSPE-PEG-Tyr, respectively. To synthesize these conjugates by coupling reaction, 102 μmol of Dopa·HCl, Ser·HCl, or Tyr was dissolved in 3 mL of anhydrous *N*,*N*-dimethylformamide (DMF) containing 102 μmol of TEA, into which 34 μmol of DSPE-PEG-NHS was added, followed by 24 h of reaction under the protection of nitrogen at room temperature. The reaction mixture was purified by dialysis (molecular weight cutoff, 1000 Da) against deionized water for 24 h. The final product was collected by freeze-drying. An antioxidant and anti-inflammatory material (TPCD) was synthesized according to previously reported methods[67].

^{1}H NMR spectra were conducted on a spectrometer operating at 600 MHz (DD2, Agilent). Fourier-transform infrared (FTIR) spectra were recorded on a PerkinElmer FTIR spectrometer (100 S). UV−Vis spectroscopy was recorded on a TU-1901 spectrophotometer (Beijing Purkinje General Instrument Co., Ltd., China).

2.3. Preparation of various nanoparticles

A modified nanoprecipitation/self-assembly method was employed to fabricate PLGA nanoparticles (defined as PN) and TPCD nanoparticles (defined as TN). Briefly, lecithin (6 mg) and DSPE-PEG (9 mg) were dissolved in 0.6 mL of ethanol, into which 15 mL of deionized water was added. The obtained mixture was heated to 65 °C for 1 h. Then, an acetonitrile solution (5 mL) containing 50 mg of PLGA or methanol solution (5 mL) containing 50 mg of TPCD was added dropwise into the above preheated aqueous solution, followed by stirring for 2 h at room temperature. The remaining organic solvent was removed by vacuum evaporation. Following similar procedures, PLGA or TPCD nanoparticles based on DSPE-PEG-Dopa, DSPE-PEG-Ser, or DSPE-PEG-Tyr were fabricated, which are defined as DPN (PLGA/DSPE-PEG-Dopa nanoparticles), SPN (PLGA/DSPE-PEG-Ser nanoparticles), TPN (PLGA/DSPE-PEG-Tyr nanoparticles), DTN (TPCD/DSPE-PEG-Dopa nanoparticles), STN (TPCD/DSPE-PEG-Ser nanoparticles), and TTN (TPCD/DSPE-PEG-Tyr nanoparticles), respectively. Similarly, Ac2-26-loaded TPCD nanoparticles based on DSPE-PEG-Tyr (defined as ATTN) and different nanoparticles labeled with Cy5 or Cy7.5 were produced.

2.4. Characterization of nanoparticles

The size, size distribution, polydispersity index (PDI), and zeta potential of different nanoparticles were examined by a Malvern Zetasizer NanoZS instrument at 25 °C. Scanning electron microscopy (SEM) was conducted on a FIB-SEM microscope (Crossbeam 340, Zeiss, Germany). Transmission electron microscopy (TEM) was performed using a JEM-1400 PLUS microscope (JEOL, Japan). The loading contents of FITC-Ac2-26, Cy5, or Cy7.5 in different nanoparticles were quantified by a fluorescence spectrophotometer (F-7000, Hitachi). In addition, the stability of different nanoparticles in deionized water, fetal bovine serum, or simulated gastric/intestinal fluids was determined by measuring the particle size at 2 h after incubation.

2.5. ROS/MPO-triggerable aggregation of nanoparticles in vitro

Various nanoparticles including PN, DPN, SPN, or TPN based on PLGA were separately incubated with a mixed solution of H_2O_2 and MPO for 8 h. Then their size and PDI values were determined by dynamic light scattering. Through similar procedures, the size changes of PN and TPN at different concentrations were examined upon incubation with 1 mmol/L H_2O_2 and 10 μg/mL MPO. In addition, time-dependent changes in the diameter of PN and TPN at 2.0 mg/mL was detected upon incubation with different concentrations of H_2O_2 and 10 μg/mL MPO. TEM and SEM images of different nanoparticles, including PN, DPN, SPN, TPN, TN, DTN, STN, and TTN, were also acquired before and after incubation with H_2O_2 (1 mmol/L) and MPO (10 μg/mL).

2.6. Measurement of ROS-scavenging capability of TPCD

To examine the H_2O_2-scavenging capability of TPCD, different concentrations of TPCD (varying from 0.5, 1.0, 2.0, 4.0, to 8.0 mg/mL) were incubated in 2 mL of PBS containing 50 mmol/L H_2O_2 at 37 °C for 24 h in dark. The concentration of remaining H_2O_2 was quantified by the Hydrogen Peroxide Detection Kit (Nanjing Jiancheng Bioengineering Institute, China), and the H_2O_2-scavenging capacity was calculated.

To detect the free radical-scavenging capability of TPCD, 0.1 mL of a fresh solution of DPPH · (100 μg/mL) was incubated in 0.2 mL of methanol containing different concentrations of TPCD (from 0, 0.063, 0.125, 0.25, 0.5, 1.0, to 2.0 mg/mL) in dark. Subsequently, the absorbance at 520 nm was detected *via* UV−Vis spectroscopy at the predetermined time points.

2.7. In vitro release tests

In brief, 10 mg of freshly fabricated FITC-Ac2-26-loaded nanoparticles were dispersed in 40 mL of PBS (0.01 mol/L, pH 7.4) with or without 2.5 mmol/L H_2O_2. At predetermined time points, 1 mL of medium was withdrawn, and the same volume of medium was supplemented. After the release medium was centrifuged at 20,000×*g* (Eppendorf) for 15 min, the concentration of FITC-Ac2-26 in the supernatant was determinate by fluorescence spectrophotometry.

2.8. Cellular uptake of nanoparticles

RAW264.7 cells (3×10^5 cells per well) or Caco-2 cells (3×10^5 cells per well) were cultured in 12-well plates overnight. Then, cells were incubated with Cy5-labeled various nanoparticles at 100 μg/mL for 4 h. The cells were then washed with PBS and harvested for flow cytometric analysis (BD FACSCelesta).

Cellular uptake of TTN aggregates was also examined in RAW264.7 macrophages. In this case, Cy5-TN and Cy5-TTN were pretreated with 10 μg/mL MPO and 1 mmol/L H_2O_2 for 0.5 h. Then the aggregated nanoparticles were collected and their cellular internalization in RAW264.7 cells was examined by confocal laser scanning microscopy (CLSM) after 4 h of incubation.

2.9. *Studies on intracellular ROS generation in RAW264.7 cells*

RAW264.7 cells were seeded into a 12-well plate (3×10^5 cells per well) and cultured overnight. Then cells in experimental groups were stimulated with PMA at 200 ng/mL, and simultaneously treated with 100 μg/mL TTN, 100 μg/mL ATTN (containing 272 ng/mL Ac2-26), and 272 ng/mL Ac2-26 for 4 h at 37 °C, respectively. The normal control group was only treated with medium, while cells in the model group were induced with PMA alone. After the cells were incubated with 10 μmol/L DCFH-DA for 25 min, fluorescence intensities were measured by flow cytometry. For direct observation of fluorescence by confocal microscopy, the aforementioned procedures were similarly performed. In this case, RAW264.7 cells were seeded in glass-bottom cell culture dishes and cell nuclei were stained with DAPI.

2.10. *In vitro anti-inflammatory activity*

RAW264.7 cells were seeded into a 12-well plate (4×10^5 cells per well) and cultured overnight. Then cells were treated with LPS (200 ng/mL) and various nanoparticles or free Ac2-26. After 6 h of incubation, the supernatant was collected to measure the tumor necrosis factor (TNF)-α concentration by ELISA.

In a separate study, TN and TTN were pretreated with 10 μg/mL MPO and 1 mmol/L H_2O_2 for 0.5 h. Then the aggregated nanoparticles were collected and their effect on the expression of TNF-α

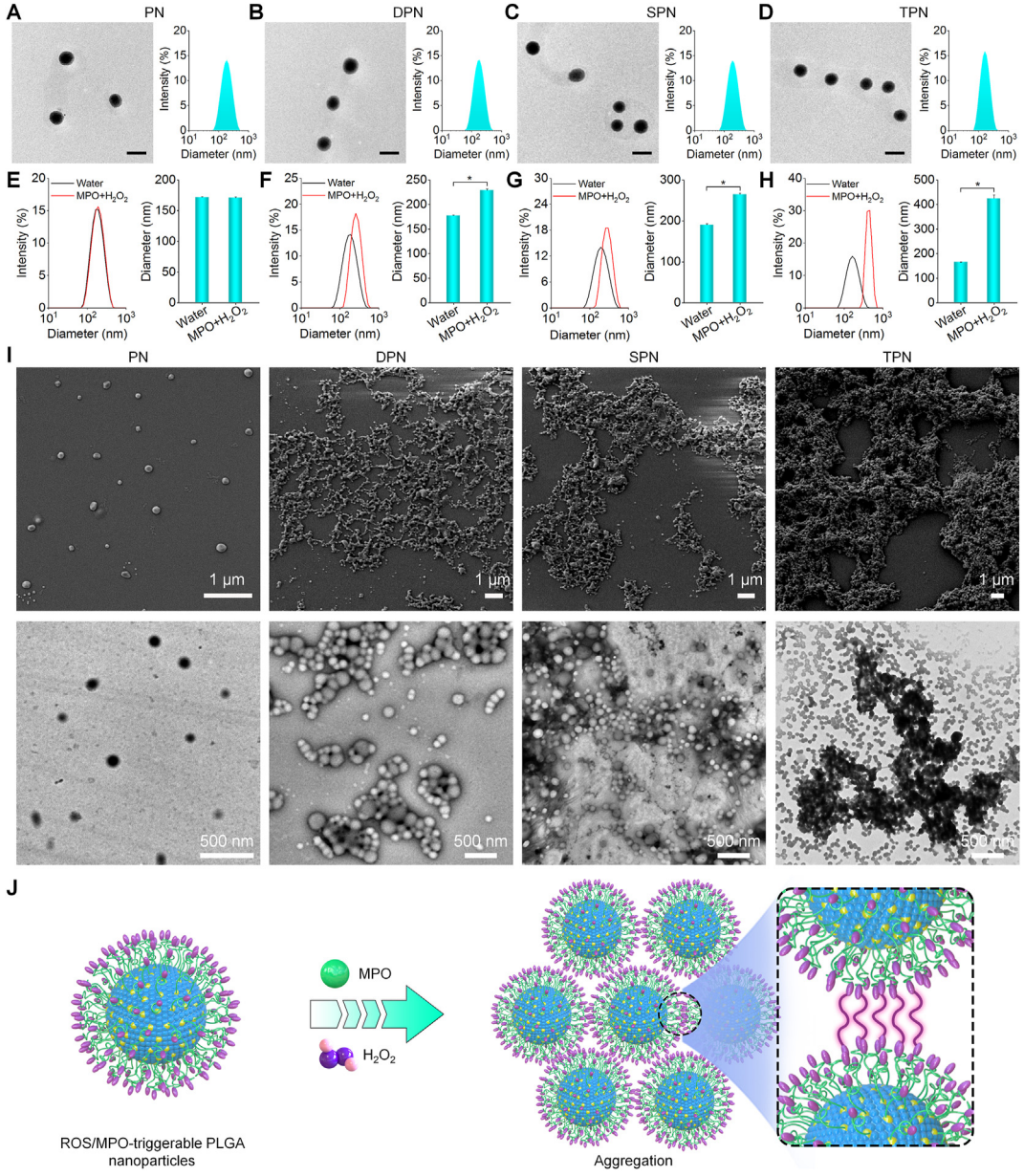

Figure 2 *In vitro* ROS/MPO-triggered aggregation of different PLGA nanoparticles decorated with varied phenolic moieties. (A–D) TEM images (left) and size distribution profiles (right) of PN (A), DPN (B), SPN (C), and TPN (D). Scale bars, 200 nm. (E–H) Size distribution profiles and mean diameters of PN (E), DPN (F), SPN (G), and TPN (H) in deionized water in the absence or presence of H_2O_2 (2.5 mmol/L) and MPO (10 μg/mL). (I) SEM (upper) and TEM (lower) images of different nanoparticles after incubation with H_2O_2 and MPO. (J) Schematic illustration of ROS/MPO-triggered aggregation of surface-functionalized PLGA nanoparticles. Data are presented as mean ± SE ($n = 3$). *$P < 0.05$.

in LPS-stimulated RAW264.7 cells was tested after 6 h of incubation.

2.11. Animals

All animal experiments were conducted in accordance with the Guide for the Care and Use of Laboratory Animals recommended by the National Institutes of Health. All procedures and experimental protocols were approved by the Animal Ethics Committee at Army Medical University (Chongqing, China). Male C57BL/6 J mice (19−21 g) and female BALB/c mice (19−21 g) were obtained from the animal center of the Army Medical University. All animals were acclimatized for a week before further experiments.

2.12. ROS/MPO-triggerable aggregation of nanoparticles in colonic homogenates of colitis mice

Acute colitis in C57BL/6 mice was induced by drinking water containing 3% (*w*/*v*) DSS for 7 days. Colon tissues from colitis mice were isolated and homogenized in cold PBS. The supernatant was collected after centrifugation at 12,000 rpm (Eppendorf) for 10 min to obtain colonic homogenates. Then freshly prepared nanoparticles (PN, DPN, SPN, or TPN) were incubated with the colonic homogenate. At predetermined time points, the mean size and PDI values of different nanoparticles were measured.

2.13. Stability of Ac2-26 in physiological fluids

Trypsin-containing PBS at pH 7.4 was prepared to simulate the intestinal fluid. In addition, fluids simulating the gastrointestinal conditions were prepared using homogenates of mouse gastrointestinal tissues. To this end, male C57BL/6 J mice were sacrificed, and the stomach and colon tissues were excised. After washing with cold PBS, the supernatant was collected after centrifugation. On the other hand, the stomach and colon tissues were homogenized in ice-cold PBS, and the obtained homogenates were centrifuged at low temperature to collect the supernatant. Subsequently, 200 μL of aqueous solution containing ATTN or free Ac2-26 was incubated at 37 °C for 2 h in 0.2 mL of various fluids, including gastric fluid, simulated gastric fluid, simulated intestinal fluid, colonic fluid, as well as stomachic and colonic homogenates. Then Ac2-26 in ATTN was extracted by methanol. The contents of Ac2-26 were quantified by high performance liquid chromatography (HPLC).

2.14. Study on the distribution of nanoparticles in mice with DSS-induced colitis

Acute colitis in C57BL/6 J mice was induced by receiving 3% DSS supplemented in drinking water for 7 days. Various Cy7.5-labeled nanoparticles, including Cy7.5-PN, Cy7.5-DPN, Cy7.5-SPN, Cy7.5-TPN, Cy7.5-TN, Cy7.5-DTN, Cy7.5-STN, and Cy7.5-TTN were separately administered by oral gavage, at the dose of 0.04 mg of Cy7.5 in each mouse. In addition, healthy mice were used as the normal control. At defined time points, the colon segment and major organs (heart, liver, spleen, lung, and kidney) were isolated for analysis. *Ex vivo* imaging was performed using a living imaging system (IVIS Spectrum, PerkinElmer, USA). The radiant efficiency was analyzed by the Living Imaging software. In another cohort study, time-dependent tissue distribution profiles of orally delivered Cy5-TPN in mice with DSS-induced colitis were examined through similar procedures.

2.15. Examination on the localization of nanoparticles in the inflamed colon by confocal microscopy

First, acute colitis was induced in mice as aforementioned. After 7 days, mice were orally administered with Cy5-PN, Cy5-DPN, Cy5-SPN, or Cy5-TPN, respectively. After 16 h, mice were euthanized. For confocal microscopy imaging, colonic tissues of 0.5 cm in length were isolated, embedded in Tissue-Tek O.C.T. Compound, and frozen at −20 °C. After 7-μm cryosections were stained with DAPI, images were taken *via* a Zeiss confocal microscope.

2.16. Treatment of DSS-induced acute colitis in mice

Acute colitis in mice was induced as mentioned above. First, efficacies of TN at different doses were examined. To this end, mice were randomly assigned into different groups. Healthy mice in the control group were not treated, while colitis mice in the model group were orally administered with saline. Colitis mice in the TN groups were separately treated with TN at 9, 18, 35, 70, 140, and 280 mg/kg by oral gavage one time each day. In a separate study, we compared therapeutic effects of TN and PN after oral administration. In this aspect, colitis mice were randomized to three groups: a saline-treated group, a PN-treated group (at 35 mg/kg), and a TN-treated group (at 35 mg/kg). Healthy mice in the normal control group were untreated. In another cohort study, animals were randomized into 4 groups: mice untreated in the normal group (Normal), colitis mice treated with saline (Colitis), colitis mice treated with TN at 35 mg/kg (TN), and colitis treated with 35 mg/kg of TTN (TTN). All different formulations were administered daily by oral gavage. To evaluate *in vivo* efficacies of Ac2-26-loaded TPCD nanoparticles, colitis mice were randomly assigned into 4 groups, which were orally treated with saline, free Ac2-26, TTN (at 35 mg/kg), or ATTN (at 35 mg/kg), respectively. The dose of Ac2-26 was 95.2 μg/kg for all Ac2-26-containing formations. Healthy mice without treatment were used in the normal control group.

Regardless of different studies, the similar procedures were followed during and after different treatments. Behaviors of mice were monitored every day during treatment, and changes in the body weight were recorded. After 7 days, mice were euthanized and different tissues and organs were excised for further analyses.

2.17. Evaluations of therapeutic effects of different nanoparticles on colitis

After different treatments, mice were euthanized and the colons (from the cecum to the rectum) were excised. The colon length was measured. Then, 0.5 cm of the distal section was used for histological assessment and immunofluorescence staining. The rest colonic tissue was homogenized and used for quantifying the levels of TNF-α, interleukin-1β (IL-1β), MPO, and hydrogen peroxide. After centrifugation at 10,621×*g* (Eppendorf) for 10 min at 4 °C, the levels of TNF-α, IL-1β, and MPO in the supernatant were measured by ELISA. The levels of hydrogen peroxide were quantified by the Hydrogen Peroxide Detection Kit.

The protein concentration in the supernatant was quantified by using the BCA Protein Assay Kit (Beyotime Biotechnology).

2.18. Histological assessment

Briefly, 0.5 cm of the distal colon was fixed with 4% (*v*/*v*) buffered formalin and paraffin-embedded. Then 7-μm thick tissue sections were prepared and stained by hematoxylin−eosin (H&E) or Periodic Acid-Schiff (PAS). Histological images were acquired by optical microscopy.

2.19. Immunofluorescence analysis of colonic tissues

Sections of colonic tissues were fixed with 4% paraformaldehyde, embedded in paraffin, blocked with 3% bovine serum albumin, and then incubated with antibody to occludin at 4 °C overnight. Subsequently, the slices were incubated with the secondary antibody of FITC-conjugated goat anti-rat IgG for 50 min at room temperature in dark, while nuclei were stained with DAPI. Then fluorescence observation of cryosections was conducted by confocal microscopy.

2.20. Mini-endoscopic imaging

An endoscope video system for mice was utilized to observe the DSS-induced colonic mucosal damage directly. After various treatments, mice were anesthetized by isoflurane inhalation (RWD Life Sciences, China). Endoscopic imaging was performed using a miniature endoscope and digitally recorded *via* a tri-chip camera (Karl Storz, Germany).

2.21. Flow cytometry analysis of inflammatory cells in colonic tissues

Colonic tissues were excised, thoroughly washed, and cut into small pieces. To remove the epithelial layer, the tissues were incubated with HBSS containing 1 mmol/L dithiothreitol and 5 mmol/L EDTA at 37 °C for 30 min. After centrifugation, the epithelium-containing supernatant was discarded. The remaining tissue was washed with HBSS twice, minced into small pieces, and further dissociated in digestion buffer containing RPMI, 1.5 mg/mL collagenase type II, 0.5 mg/mL Dispase II, and 1.2% fetal bovine serum (FBS), followed by constant stirring at 37 °C for 45 min. Single-cell suspensions were obtained by passing the suspensions through 70-μm cell strainers. The cells were stained with APC-conjugated rat anti-mouse CD11b antibody, PE-conjugated rat anti-mouse Ly6G antibody, FITC-conjugated anti-mouse F4/80 antibody, or isotype controls at 4 °C for 20 min. Flow cytometric analysis was performed on a BD FACSCanto II flow cytometer. Data were analyzed using the FlowJo v10 software (BD Biosciences).

2.22. In vivo intestinal permeability assay

Acute colitis was induced in mice as aforementioned. After 7 days of different treatments, mice were fasted for 4 h and then orally administered with 0.5 mg/g of FITC-labeled dextran (3−5 kDa). After 4 h, blood was collected and centrifuged at 10,000×*g* (Eppendorf) for 10 min, and FITC fluorescence of the supernatant was measured (with excitation wavelength at 485 nm and emission wavelength at 520 nm). The concentration of FITC-dextran was calculated using a standard curve obtained by diluting FITC-dextran in non-treated plasma with PBS (1:3, *v*/*v*).

2.23. In vitro anti-migration activity of Ac2-26-containing nanoparticles in inflammatory cells

A Transwell assay was performed to examine the anti-migration activity of Ac2-26-containing nanoparticles (*i.e.*, ATTN). The effect of ATTN on the migration of RAW264.7 murine macrophages induced by MCP-1 was first investigated. Specifically, RAW264.7 cells (5×10^5 cells) were separately incubated with free Ac2-26, TTN (100 μg/mL), and ATTN (100 μg/mL) on the upper chamber. Then 0.5 mL of growth medium containing 40 ng of MCP-1 was filled in the lower chamber. No MCP-1 and different formulations were added in the control group, while cells in the model group were induced with MCP-1 alone. After 24 h, cells on the upper side of each insert were gently removed with a cotton swab, and cells on the lower side of each insert were fixed with 4% paraformaldehyde and stained with 0.1% crystal violet. After staining, 5 randomly selected images of migrated cells per high-power field (HPF, 20 × 10) were acquired and counted by optical microscopy.

In vitro anti-migration activity of different nanoparticles was also evaluated in activated neutrophils. To collect activated neutrophils, 1 mL of PBS containing thioglycollate (3.0 wt%) was intraperitoneally (i.p.) administrated to BALB/c mice. After 4 h, mice were euthanized and 5 mL of sterile PBS was injected into the peritoneal cavity. Then peritoneal exudates/lavage containing neutrophils (>90%) was collected and the suspension was centrifuged at 1680 rpm (Eppendorf) for 10 min. Subsequently, the isolated activated neutrophils (5×10^5 cells) were treated with free Ac2-26, TTN (100 μg/mL), or ATTN (100 μg/mL). In the positive control group, no formulations were added. The lower chamber was filled with 0.5 mL of growth medium containing 10% FBS. After 1 h of incubation, 5 images of migrated cells in the lower chamber were captured and counted by optical microscopy.

2.24. Liver targeting of ROS-triggerable nanoparticles in mice with APAP-induced hepatic injury

Male C57BL/6 J mice were fasted for 15 h before experimentation. Then mice were i.p. injected with acetaminophen (APAP) at 200 mg/kg. At 6 h after stimulation with APAP, Cy5-labeled nanoparticles including Cy5-PN, Cy5-DPN, Cy5-SPN, Cy5-TPN, Cy5-TN, or Cy5-TTN were i.v. administered at 0.5 mg/kg of Cy5. Healthy mice in the control group received saline alone. After 16 h, livers, blood samples, and other major organs (including the heart, spleen, lung, and kidney) were isolated and imaged on an IVIS Spectrum system. The radiant efficiency was analyzed by the Living Imaging software. In another study, time-dependent blood and liver distribution profiles of i.v. delivered Cy5-PN or Cy5-TPN in mice with APAP-induced hepatic injury were examined through similar procedures.

2.25. Therapeutic effects of different nanoparticles in the treatment of APAP-induced hepatic injury

APAP-induced hepatic injury in mice was established as above mentioned. The injured mice were randomly divided into 3 groups. After 6 h, mice were i.v. injected with saline, TN (at 0.5 mg/kg), and TTN (at 0.5 mg/kg), respectively. Healthy mice in

the normal group received saline alone. At 16 h after different treatments, mice were euthanized. A part of the liver tissue was fixed with paraformaldehyde for histopathological analysis. The remaining liver tissue was homogenized in cold PBS and then centrifuged at 10,621×*g* at 4 °C for 10 min. The supernatant was collected for quantification of the levels of H_2O_2, MPO, TNF-α, and IL-1β. Major organs including the heart, spleen, lung and kidney were isolated and histopathological sections were prepared and stained with H&E.

For apoptosis analysis, tissue sections of livers were fixed with 4% paraformaldehyde, embedded in paraffin, treated with protease K (G1205, Servicebio), permeabilized with 0.1% Triton, and stained with terminal deoxynucleotidyl transferase dUTP nick end labeling (TUNEL, G1501, Servicebio) for immunofluorescence analysis.

2.26. *Lung targeting of ROS-triggerable nanoparticles in mice with LPS-induced acute lung injury*

Female BALB/c mice were subjected to intratracheal inoculation with 50 μL of PBS containing LPS at 1.0 mg/mL to induce acute lung injury (ALI). At 0.5 h after stimulation with LPS, Cy5-labeled nanoparticles including Cy5-PN, Cy5-DPN, Cy5-SPN, and Cy5-TPN were i.v. administered at 0.5 mg/kg of Cy5. Healthy mice in the control group were treated by i.v. injection of saline. After 16 h, the lung and other major organs as well as blood samples were collected for *ex vivo* imaging with an IVIS Spectrum system.

2.27. *ROS/MPO-triggered aggregation of nanoparticles in lung and liver homogenates*

Lung tissues from mice with LPS-induced ALI were isolated and homogenized in cold PBS. The supernatant was collected after centrifugation at 12,000 rpm (Eppendorf) for 10 min to obtain lung homogenates. The liver homogenate was prepared using the liver collected from mice with APAP-induce acute liver injury. Then freshly prepared nanoparticles (PN or TPN) were separately incubated with the lung or liver homogenate. After 2 h, the mean diameter of different nanoparticles was measured.

2.28. *Acute toxicity evaluation of TTN*

Male C57BL/6 J mice were randomly divided into three groups ($n = 5$). TTN was orally administered at 175 or 350 mg/kg for 7 days, while mice in the control group were given saline by oral gavage. The body weight of mice and their behaviors were monitored each day. On Day 14, animals were euthanized, and blood samples were collected for hematological analysis. The major organs including the heart, liver, spleen, lung, kidney, stomach, and intestine were excised and weighed. Histological sections were prepared and stained with H&E.

2.29. *Statistical analysis*

All data are presented as mean ± standard error of the mean (SE). Statistical analyses were performed with the software of SPSS20.0 using independent-samples *t*-test for experiments with two groups, and one-way ANOVA for experiments consisting of more than two groups. A value of $P < 0.05$ was assessed as statistically significant.

3. Results and discussion

3.1. *Engineering of PLGA nanoparticles with different phenolic coatings*

As previously demonstrated, phenolic compounds can be polymerized in the presence of H_2O_2 and relevant catalytic enzymes[56,58,60]. To develop nanoparticles with ROS-triggered polymerizable or clustering capability, three representative phenolic compounds including dopamine (Dopa), serotonin (Ser), and tyramine (Tyr) were used as functional moieties due to their broad availability, good safety, and easy conjugation (Supporting Information Fig. S1). Specifically, Dopa, Ser, and Tyr were separately conjugated with 1,2-distearoyl-*sn*-glycero-3-phosphoethanolamine-*N*-[hydroxysuccinimide (polyethylene glycol)-2000] (DSPE-PEG-NHS) to afford three DSPE-PEG derivatives DSPE-PEG-Dopa, DSPE-PEG-Ser, and DSPE-PEG-Tyr, respectively. The successful synthesis of different DSPE-PEG derivatives was confirmed by ^{1}H NMR and Fourier-transform infrared (FTIR) spectroscopy (Supporting Information Fig. S2).

Then nanoparticles with various phenolic coatings were constructed based on PLGA, a Food and Drug Adiminitration (FDA)-approved biodegradable polymer, by a modified nanoprecipitation/self-assembly method[48]. PLGA nanoparticles prepared in the presence of DSPE-PEG, DSPE-PEG-Dopa, DSPE-PEG-Ser, and DSPE-PEG-Tyr are defined as PN, DPN, SPN, and TPN, respectively (Fig. 1B). For the obtained nanoparticles, examination by transmission electron microscopy (TEM) and dynamic light scattering (DLS) showed spherical morphology with a narrow size distribution, regardless of their different surface phenolic coatings (Fig. 2A−D). The average diameter was 173 ± 1, 178 ± 1, 190 ± 3, and 165 ± 0.3 nm for PN, DPN, SPN, and TPN, respectively.

3.2. *In vitro ROS/MPO-triggered aggregation of different PLGA nanoparticles*

To examine whether PLGA nanoparticles with different phenolic coatings exhibit inflammation/oxidative stress-triggered clustering or aggregation behaviors, their size changes were evaluated after incubation in buffers containing ROS/MPO, since these oxidative/pro-inflammatory mediators are generally highly expressed during inflammatory responses. The hydrodynamic diameter of PN was almost unchanged after incubation with H_2O_2 and MPO, compared to that in deionized water (Fig. 2E). By contrast, the diameter of DPN, SPN, and TPN (at 2.0 mg/mL) significantly increased after incubation with H_2O_2 and MPO (Fig. 2F−H), which was 229 ± 3, 265 ± 3, and 425 ± 14 nm, respectively. This indicated clustering or aggregation of PLGA nanoparticles with phenolic coatings. Moreover, we found that the diameter of TPN was positively correlated with the concentration of H_2O_2 and nanoparticles (Supporting Information Fig. S3). Even at a relatively low concentration of 0.2 mg/mL, a significant increase in the diameter of TPN was still observed after incubation with 1 mmol/L H_2O_2 and 10 μg/mL MPO. By contrast, the diameter of PN was almost unchanged under various conditions. Further observation by scanning electron microscopy (SEM) and TEM confirmed H_2O_2/MPO-triggered aggregation of PLGA nanoparticles with phenolic functionalization (Fig. 2I). In this case, notable clustering and assembly of DPN, SPN, and TPN were observed, while PN and phenolic compound-functionalized PLGA nanoparticles before incubation remained well-dispersed, showing

spherical single nanoparticles (Supporting Information Fig. S4). Accordingly, PLGA nanoparticles with surface phenolic moieties can be effectively triggered by the inflammatory microenvironment to form nanoparticle assemblies. According to previous studies, ROS in combination with peroxidases can mediate oxidation of phenolic moieties (such as tyrosine and dopamine)[56,65,66], thereby resulting in polymerization by proton-coupled electron transfer reactions. Mechanistically, H_2O_2/MPO-mediated assembly of DPN, SPN, or TPN can be attributed to the oxidization of phenolic groups on the surface of these nanoparticles, and the produced free radicals on different nanoparticles will be oligomerized or polymerized to form large aggregates (Fig. 2J).

3.3. In vivo amplified accumulation of phenolic compound-functionalized nanoparticles at the inflamed colon by ROS/MPO-triggered aggregation

Subsequently, *in vivo* studies were performed to validate whether ROS/MPO-triggered aggregation of PLGA nanoparticles can enhance their accumulation in inflammatory and oxidative tissues. In view of the pivotal role of ROS-mediated oxidative stress in the pathogenesis of inflammatory bowel disease (IBD)[27], we first examined the accumulation of various fluorescent-labeled PLGA nanoparticles at the injury site of the inflamed colon. Colitis in mice was induced by oral administration of dextran sulfate sodium (DSS) in drinking water for 7 days (Fig. 3A)[28]. At 16 h after oral administration, *ex vivo* imaging showed significantly higher fluorescent signals in colons from mice delivered with Cy7.5-DPN, Cy7.5-SPN, and Cy7.5-TPN, as compared to those from Cy7.5-PN-treated mice (Fig. 3B). Nevertheless, three phenolic moiety-coated nanoparticles showed comparable distribution in the inflamed colon. Moreover, phenol-decorated PLGA nanoparticles displayed slightly increased distribution in typical major organs, such as the heart, liver, spleen, lung, and kidneys, which should be attributed to the enhanced absorption in the intestine (Supporting Information Fig. S5). Further fluorescence examination also revealed the enhanced targeting capability of DPN, SPN, and TPN to the inflamed colon, with more significant fluorescence in the Cy5-TPN group (Fig. 3C). Consistent with these results, the

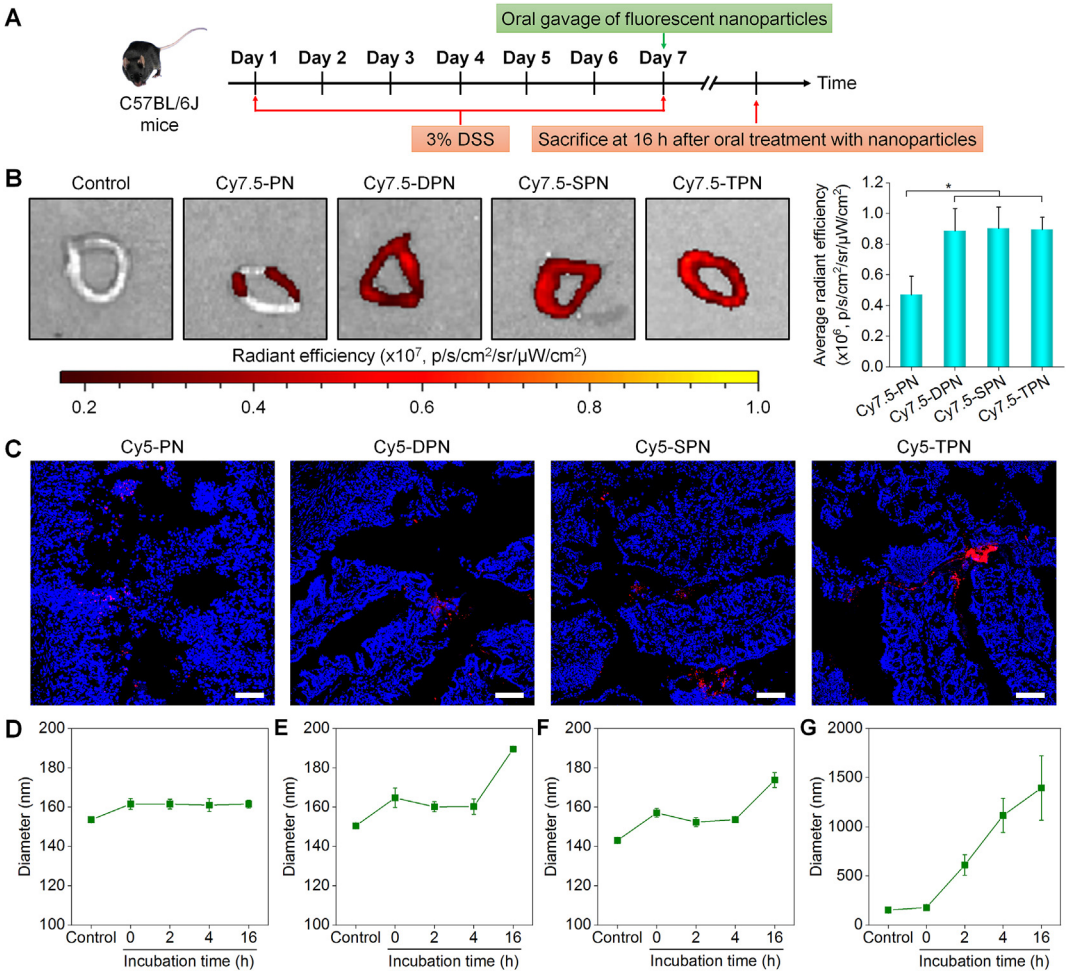

Figure 3 Enhanced targeting capability to inflammatory and oxidative tissues by *in-situ* triggered aggregation of different functional PLGA nanoparticles. (A) Schematic illustration of treatment regimens. (B) *Ex vivo* fluorescence images (left) and quantitative analysis (right) of fluorescence intensities in colonic tissues from colitis mice at 16 h after oral administration of different Cy7.5-labeled PLGA nanoparticles. (C) Fluorescence images of cryosections indicating the accumulation of different Cy5-labeled PLGA nanoparticles in the colonic tissues of mice with DSS-induced colitis at 16 h after oral administration. Nuclei were labeled with DAPI. Scale bars, 100 μm. (D–G) Changes in the diameter of PN (D), DPN (E), SPN (F), and TPN (G) after incubation with colonic homogenates of colitis mice for different periods of time. Data are presented as mean ± SE ($n = 3$). *$P < 0.05$.

mean diameter of different phenol-decorated PLGA nanoparticles notably increased after incubation with colonic homogenates of colitis mice for different time periods, while the PN group only exhibited slight changes (Fig. 3D−G). Of note, PN and TPN displayed good colloidal stability and showed comparable diameter in the simulated gastric and intestinal fluids (Supporting Information Fig. S6), which could not affect ROS/MPO-triggered aggregation of functionalized nanoparticles. This suggested that both PN and TPN are stable under normal physiological conditions of the gastrointestinal tract, mainly due to the presence of peripheral PEG chains on nanoparticles that can considerably prevent adhesion and binding of biomolecules by a hydration effect. In a separate study, we found that the colonic accumulation of orally delivered Cy5-TPN can maintain for at least 36 h in mice with DSS-induced colitis (Supporting Information Fig. S7). The enhanced accumulation and retention of TPN should be mainly due to the aggregation of Tyr-functionalized nanoparticles at the inflammatory sites upon triggering by ROS/MPO.

Based on the above promising results, we investigated whether phenol-decorated nanoparticles derived from other materials also display enhanced targeting to inflamed sites. To this end, a bioactive material (*i.e.*, TPCD) was first synthesized by sequentially conjugating Tempol and phenylboronic acid pinacol ester onto β-CD[67], which was confirmed by FTIR and ^{1}H NMR spectroscopy (Supporting Information Fig. S8A and S8B). Calculation based on the ^{1}H NMR spectrum suggested that each TPCD molecule contains approximately 2 Tempol and 5 phenylboronic

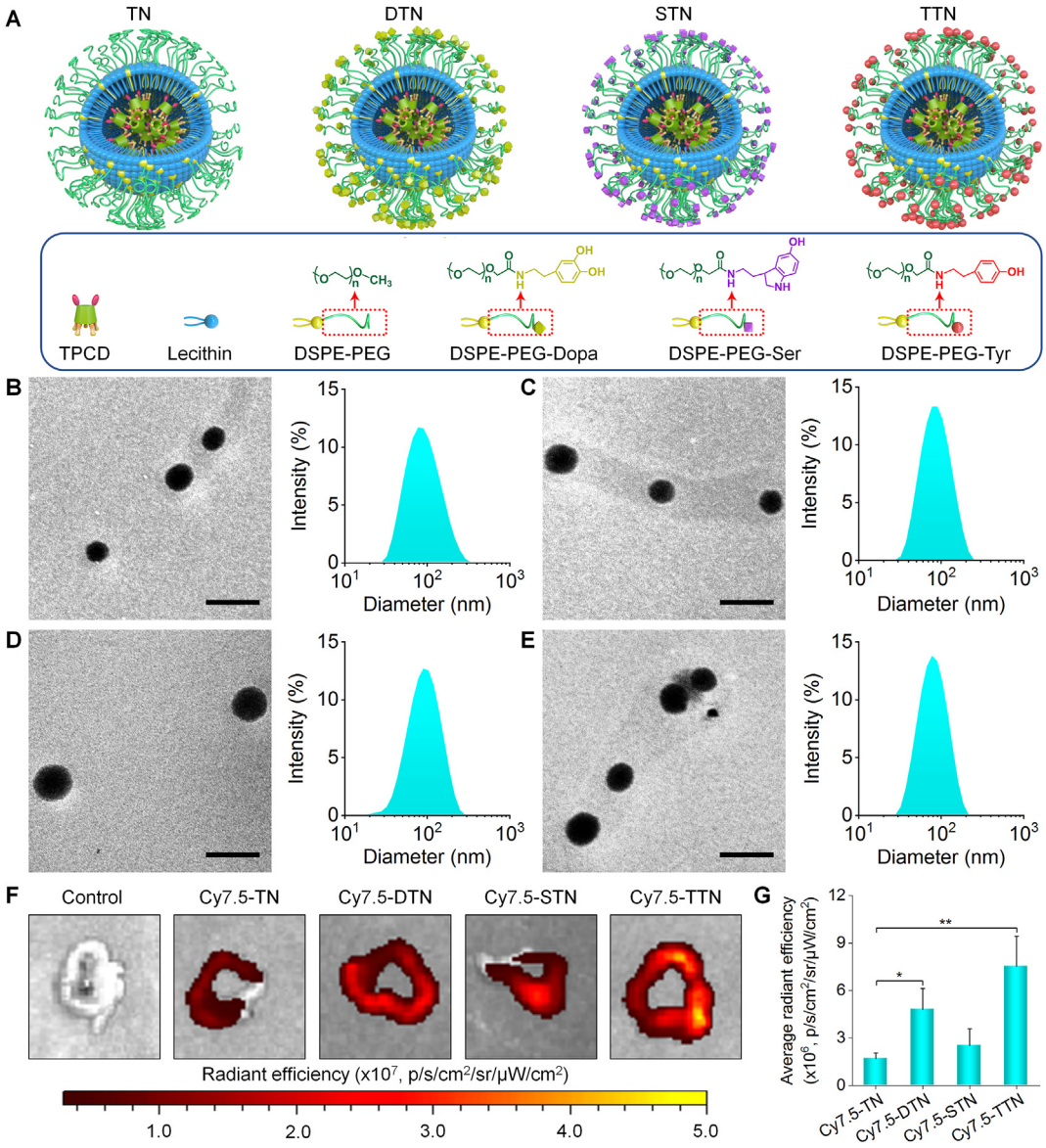

Figure 4 Engineering of functionalized TPCD nanoparticles and enhanced targeting capability to colonic tissues of colitis mice. (A) Schematic illustration of various TPCD nanoparticles. (B−E) Representative TEM images (left) and size distribution profiles (right) of TN (B), DTN (C), STN (D), and TTN (E). Scale bars, 200 nm. (F and G) *Ex vivo* fluorescence images (F) and quantitative analysis (G) showing fluorescence intensities of different Cy7.5-labeled TPCD nanoparticles in colonic tissues of colitis mice at 16 h after oral administration. TN, TPCD/DSPE-PEG nanoparticles; DTN, TPCD/DSPE-PEG-Dopa nanoparticles; STN TPCD/DSPE-PEG-Ser nanoparticles; TTN, TPCD/DSPE-PEG-Tyr nanoparticles. Data are presented as mean ± SE (G, $n = 5$). *$P < 0.05$, **$P < 0.01$.

acid pinacol ester (PBAP) moieties. As expected, TPCD can efficiently eliminate different ROS, such as H_2O_2 and free radical (Fig. S8C and S8D). TPCD nanoparticles with various phenolic moieties were also prepared by the aforementioned nanoprecipitation/self-assembly method, using DSPE-PEG, DSPE-PEG-Dopa, DSPE-PEG-Ser, and DSPE-PEG-Tyr, and the obtained nanoparticles are termed as TN, DTN, STN, and TTN, respectively (Fig. 4A). All TPCD-derived nanoparticles were spherical in shape, with the mean diameter of 96 ± 3, 95 ± 2, 82 ± 1, and 86 ± 2 nm, respectively (Fig. 4B−E). Similarly, observation by SEM and TEM confirmed H_2O_2/MPO-triggered aggregation of TPCD nanoparticles with phenolic functionalization (Supporting Information Fig. S9). In this aspect, DTN, STN, and TTN showed remarkable clustering and assembly after incubation with H_2O_2 and MPO, while TN and functionalized TPCD nanoparticles before incubation were well-dispersed single particles. Then the accumulation of Cy7.5-labeled various TPCD nanoparticles at the injury site was examined in mice with DSS-induced colitis. Whereas fluorescence was detected for all TPCD nanoparticles at 16 h after oral administration, significantly high fluorescent signals were found in inflamed colons from Cy7.5-DTN and Cy7.5-TTN groups, as compared to that of the Cy7.5-TN group (Fig. 4F and G). In this case, the highest accumulation was observed for Cy7.5-TTN, *i.e.*, the Tyr-coated TPCD nanoparticles. The colonic distribution performance of TPCD nanoparticles is different from that of PLGA nanoparticles. Whereas *in vivo* tissue distribution profiles of different nanoparticles are largely determined by their size and surface chemistry, the attributes of carrier materials may also affect the *in vivo* fate of nanoparticles based on bioresponsive materials, mainly by inducing changes in their physicochemical properties. TPCD nanoparticles themselves can scavenge ROS and target inflammatory tissues, which may affect the local pathophysiological microenvironment, thereby changing the tissue distribution performance of different TPCD nanoparticles with various surface coatings. As for PLGA nanoparticles, the core-forming material does not affect the related microenvironment, and therefore their biodistribution is mainly dominated by surface chemistry. In addition to kidneys, almost similar distribution profiles in the heart, liver, spleen, and lung were observed (Supporting Information Fig. S10). In addition, ROS-responsive hydrolysis of TPCD nanoparticles can generate phenylboronic moieties that have high binding interactions with diol-containing biomolecules, thereby further promoting their accumulation at the inflammatory tissues. Together, these results unequivocally substantiated that orally delivered phenol-decorated nanoparticles derived from different carrier materials can more efficiently target the inflamed colon than nanoparticles with the PEG coating alone.

3.4. *Amplified accumulation of phenol-functionalized nanoparticles in the injured liver/lung*

Subsequently, we tested *in vivo* ROS/MPO-triggered accumulation of phenol-decorated PLGA nanoparticles in an inflammatory model of acute liver injury. Mice with acute liver injury were induced by acetaminophen (APAP)[62]. Whereas all Cy5-labeled PLGA nanoparticles showed notable accumulation in the injured liver after intravenous (i.v.) administration, phenol-coated nanoparticles (Cy5-DPN, Cy5-SPN, and Cy5-TPN) exhibited significantly higher fluorescent signals than that of Cy5-PN (Fig. 5A and B). Of note, Cy5-TPN showed the highest distribution in the injured liver. Nevertheless, Cy5-PN and Cy5-TPN displayed a similar pharmacokinetic profile in the blood (Supporting Information Fig. S11A). Consistently, the comparable diameter was found for PN and TPN after incubation in serum for 2 h (Fig. S11B). In addition, we found remarkably higher accumulation of Cy5-TPN in the injured liver than that of the healthy liver (Fig. 5C and D). Moreover, Cy5-TPN could be retained in the inflammatory liver for more than 48 h (Fig. S11C).

Further studies were performed to evaluate targeting efficiency of phenol-decorated PLGA nanoparticles in mice with lipopolysaccharide (LPS)-induced acute lung injury (ALI). It is worth noting that ALI is characterized by neutrophil-mediated inflammation, with the most severe symptom of acute respiratory distress

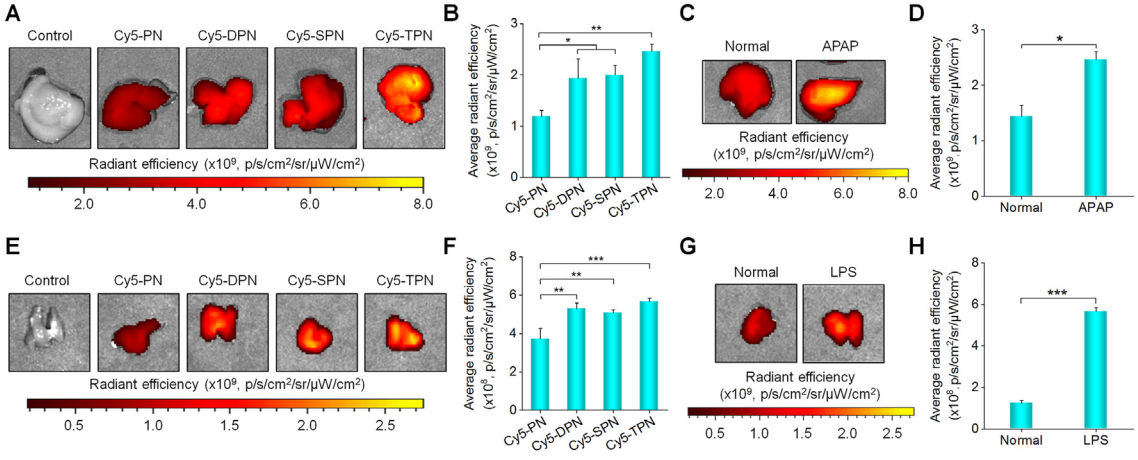

Figure 5 Enhanced accumulation of ROS/MPO-triggerable nanoparticles in oxidative and inflammatory organs in mouse models of acute liver injury and acute lung injury. (A and B) *Ex vivo* fluorescence images (A) and quantification (B) showing fluorescence intensities of different Cy5-labeled PLGA nanoparticles accumulated in the livers of mice with APAP-induced acute liver injury at 16 h after i.v. administration. (C and D) *Ex vivo* fluorescence images (C) and quantification (D) of Cy5-TPN accumulated in the livers of healthy mice or mice with acute liver injury at 16 h after i.v. administration. (E and F) Typical *ex vivo* fluorescence images (E) and quantitative analysis (F) illustrating the accumulation of different Cy5-labeled PLGA nanoparticles in the lungs of mice with LPS-induced acute lung injury at 16 h after i.v. administration. (G and H) *Ex vivo* fluorescence images (G) and quantitative analysis (H) of the lungs isolated from healthy mice or mice with acute lung injury at 16 h after treatment with Cy5-TPN. Data are presented as mean ± SE ($n = 3$). $^*P < 0.05$, $^{**}P < 0.01$, $^{***}P < 0.001$.

syndrome, thereby frequently leading to significant morbidity and mortality[68]. Consistent with the findings based on acute colitis and liver injury models, phenol-decorated PLGA nanoparticles displayed considerably higher accumulation in the injured lung than Cy5-PN, after i.v. delivery (Fig. 5E and F). Compared to Cy5-DPN or Cy5-SPN, Cy5-TPN showed a more desirable targeting effect. In addition, *ex vivo* imaging revealed a significantly higher accumulation of Cy5-TPN in the lung isolated from ALI mice than that from normal mice at 16 h after i.v. injection (Fig. 5G and H). In support of the enhanced accumulation in the injury liver and lung, we found that the diameter of TPN notably increased after 2 h of incubation with tissue homogenates of the liver or lung isolated from diseased mice, while PN only exhibited slight changes (Supporting Information Fig. S12).

In combination with the finding based on the colitis model, we can conclude that functionalization of nanoparticles with phenolic moieties (in particular Tyr) enables significant amplification of their targeting efficiency in different tissues/organs with inflammation and/or oxidative stress, resulting from ROS/MPO-induced oxidation and aggregation of functionalized nanoparticles. This pathologically triggerable aggregation effect enhanced the accumulation and prolonged the retention of nanoparticles at inflammatory sites, and therefore led to improved inflammatory tissue targeting capability. As for Tyr, it may cross-link with tyrosine residues, which are abundant in biological tissues, under inflammatory conditions, thereby further enhancing bio-adhesion and retention effects. Whereas only three representative phenolic compounds were examined in this study, we can reasonably speculate that other synthetic and natural phenolic compounds (such as gallic acid, catechin, epigallocatechin gallate, tannic acid, and caffeic acid) should also exhibit ROS-triggered polymerizable capability, since peroxidase/ROS-mediated oxidation is universal for many phenolic groups. In view of the prominent targeting effect of Tyr-decorated nanoparticles, they were employed in the following experiments to demonstrate the therapeutic advantages.

3.5. *Therapeutic effects of TPCD nanoparticles in DSS-induced acute colitis mice*

Our previous studies demonstrated that TPCD nanoparticles (TN) can serve as bioactive nanotherapies to prevent and treat acute/chronic inflammatory diseases, such as acute liver/lung injury and atherosclerosis[67]. To substantiate whether Tyr-decoration can increase *in vivo* efficacy of TN for the treatment of diseases related

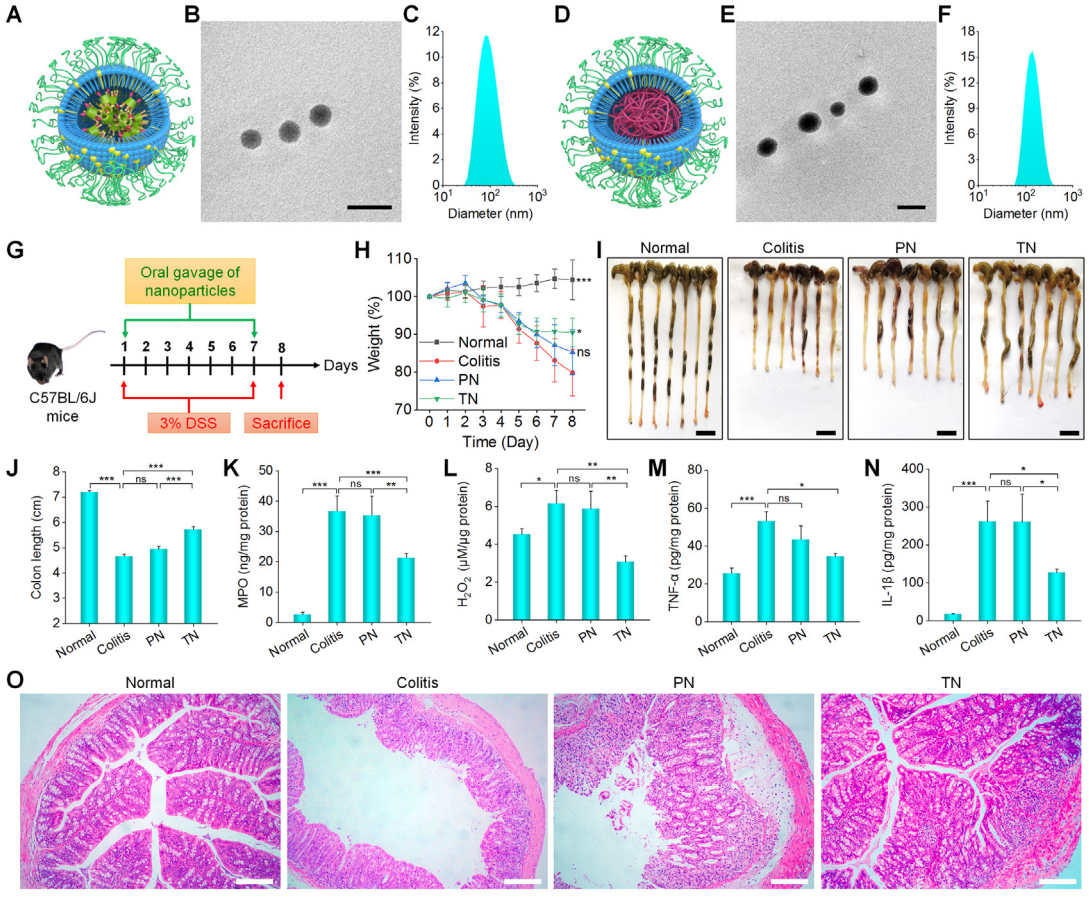

Figure 6 Therapeutic effects of TN and PN on DSS-induced acute ulcerative colitis in mice. (A–C) Schematic illustration (A), TEM image (B), and size distribution (C) of TN. (D–F) Schematic illustration (D), TEM image (E), and size distribution (F) of PN. Scale bars, 200 nm. (G) A schematic diagram of the treatment protocols. (H) Changes in the body weight of mice during 7 days of treatment. $^{*}P < 0.05$, $^{***}P < 0.001$, and ns (no significance) *versus* the colitis group. (I and J) Representative digital photos (I) and quantified lengths (J) of colonic tissues from mice after different treatments. Scale bars, 10 mm. (K–N) The expression levels of MPO (K), H_2O_2 (L), TNF-α (M), and IL-1β (N) in colonic tissues from healthy or colitis mice treated with different formulations. (O) H&E-stained histological sections of colonic tissues. Scale bars, 100 μm. Data in (H, J–N) are presented as mean ± SE (H, J, $n = 7$; K–N, $n = 6$–7). $^{*}P < 0.05$, $^{**}P < 0.01$, $^{***}P < 0.001$; ns, no significance.

to inflammation and oxidative stress, we first interrogated therapeutic effects of TN in DSS-induced acute colitis. Treatment was conducted by daily oral administration of TN at 9, 18, or 35 mg/kg for 7 Days in colitis mice, to explore dose−response effects. Mice in the model group showed significant weight loss and decreased colon length, compared to those of normal mice (Supporting Information Fig. S13A and S13C). Whereas treatment with 9 or 18 mg/kg TN showed no beneficial effects, TN at 35 mg/kg afforded beneficial results, in comparison to the colitis group. Also, DSS-treated mice had remarkably increased levels of oxidative stress-related mediators (MPO and H_2O_2) and pro-inflammatory cytokines, such as TNF-α and IL-1β, as compared to normal mice. By contrast, treatment with TN at 35 mg/kg resulted in much lower levels of MPO, H_2O_2, TNF-α, and IL-1β (Fig. S13D and S13G). Further examination of Hematoxylin and Eosin (H&E)-stained histological sections revealed severe epithelial disruption and notable inflammatory cell infiltration in the colon isolated from colitis mice (Fig. S13H). Treatment by various doses of TN attenuated colonic injuries to different degrees, and the best effect was achieved by TN at 35 mg/kg. Furthermore, we screened the optimal dosage of TN for the treatment of acute colitis in mice. In this case, different doses of TN at 35, 70, 140, or 280 mg/kg were examined. Treatment with TN at these doses effectively alleviated colitis, as implicated by reduced weight loss, improved colon length, attenuated expression of inflammatory and oxidative mediators, and less colonic tissue damage (Supporting Information Fig. S14). Nevertheless, TN at doses higher than 35 mg/kg did not afford additionally enhanced therapeutic benefits, as compared to 35 mg/kg. Accordingly, TN at 35 mg/kg was employed in further studies.

To confirm that the anti-colitis activity of TN is contributed by TPCD, we compared therapeutic effects of TN and PN at 35 mg/kg. Both TN and PN examined were spherical nanoparticles with narrow size distributions (Fig. 6A−F). Acute colitis in mice was

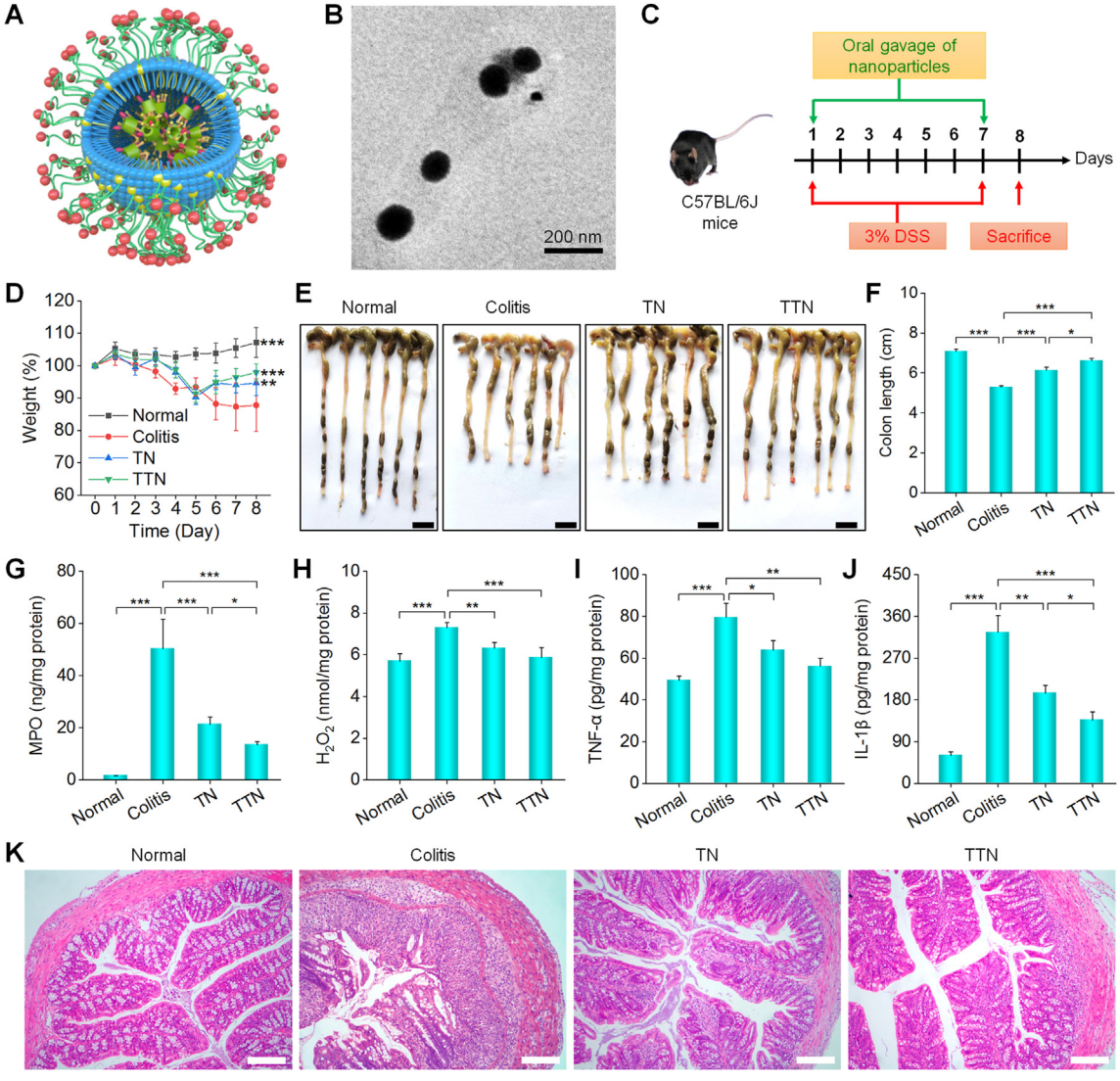

Figure 7 Potentiated therapeutic effects of Tyr-functionalized TPCD nanoparticles in mice with DSS-induced acute colitis. (A and B) Schematic (A) and a typical TEM image (B) of TTN. (C) Treatment regimens. (D) Changes in the body weight of mice during a 7-day treatment course. $^{**}P < 0.01$ and $^{***}P < 0.001$ *versus* the colitis group. (E and F) Digital photos (E) and quantified lengths (F) of colonic tissues from mice after different treatments. Scale bars, 10 mm. (G−J) The levels of MPO (G), H_2O_2 (H), TNF-α (I), and IL-1β (J) in colonic tissues isolated from healthy or colitis mice after treatment with different formulations. (K) H&E-stained histological sections of colonic tissues. Scale bars, 100 μm. All quantitative data are presented as mean ± SE (D, F, $n = 6$; G−J, $n = 5$). $^{*}P < 0.05$, $^{**}P < 0.01$, $^{***}P < 0.001$.

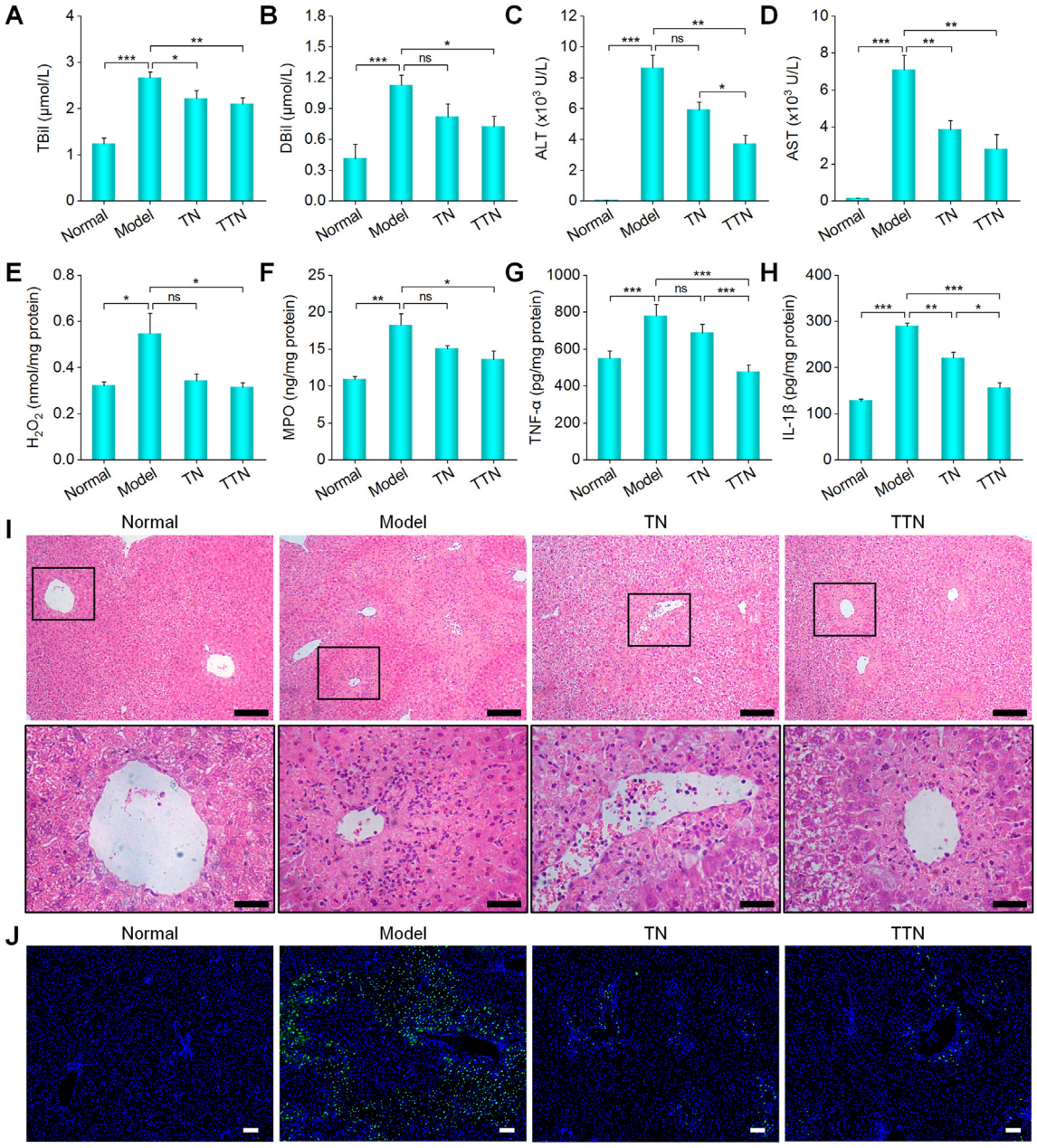

Figure 8 *In vivo* therapeutic effects of TTN in mice with APAP-induced acute liver injury. (A−D) The serum levels of TBil (A), DBil (B), ALT (C), and AST (D) for normal or diseased mice after different treatments. (E−H) The expression levels of H_2O_2 (E), MPO (F), TNF-α (G), and IL-1β (H) in the liver tissues isolated from mice treated with different formulations. (I) H&E-stained histological sections of liver tissues resected from mice subjected to different treatments. The lower panel shows high-resolution images. Scale bars, 100 μm (upper), 25 μm (lower). (J) Immunofluorescence images of liver sections stained with TUNEL. Nuclei were stained with DAPI. Scale bars, 100 μm. TBil, total bilirubin; DBil, direct bilirubin; ALT, alanine aminotransferase; AST, aspartate transaminase. Data are presented as mean ± SE ($n = 5$). *$P < 0.05$, **$P < 0.01$, ***$P < 0.001$; ns, no significance.

also induced by DSS and simultaneously treated with different formulations for 7 Days (Fig. 6G). On Day 8, TN-treated mice showed less weight loss and longer colon length in comparison to the saline-treated group (Fig. 6H−J). Also, the expression levels of MPO and H_2O_2 were markedly suppressed by treatment with TN (Fig. 6K and L). In addition, TN significantly decreased the levels of typical proinflammatory cytokines TNF-α and IL-1β (Fig. 6M and N). Therapy with PN, however, afforded no therapeutic benefits. Consistently, inspection on H&E-stained sections of colonic tissues revealed severe inflammation with loss of crypt structure, depletion of goblet cells, and extensive neutrophil infiltration in diseased mice, which were greatly improved after treatment with TN, but not PN (Fig. 6O).

Collectively, these results demonstrated that TN can serve as an effective nanotherapy for the treatment of colitis by oral delivery. Therapeutic effects of TN were mainly achieved by suppressing local inflammation and attenuating oxidative stress in the inflamed colon.

3.6. *Potentiated in vitro and in vivo biological activities of TN by Tyr decoration*

We then investigated whether decoration of TN with phenolic moieties can enhance its bioactivities. Since the aforementioned results indicated more desirable inflammation-targeting capability of Tyr-functionalized nanoparticles, Tyr-decorated TPCD nanoparticles (*i.e.*, TTN) were employed in the following studies, which were also prepared by nanoprecipitation/self-assembly (Fig. 7A and B). First, flow cytometric quantification suggested that Cy5-labeled TTN (*i.e.*, Cy5-TTN) exhibited significantly higher cellular uptake in both Caco-2 human epithelial cells and RAW264.7 murine macrophages, as compared to Cy5-labeled TN (Cy5-TN) (Supporting Information Fig. S15A and S15B). Correspondingly, TTN more effectively reduced the expression of TNF-α in LPS-stimulated macrophages than TN (Fig. S15C). Also, TTN suppressed phorbol myristate acetate (PMA)-induced ROS generation in macrophages to a much better extent than TN (Fig. S15D and S15E). In view of MPO/ROS-induced aggregation of TTN in the inflammatory microenvironment, we further examined whether TTN aggregates can be efficiently internalized by macrophages. Whereas MPO/ROS pretreatment showed no considerable effects on internalization of Cy5-TN in macrophages, notably enhanced cellular uptake was found for Cy5-TTN after preincubation with MPO and H_2O_2 (Supporting Information Fig. S16), as implicated by remarkably enhanced intracellular fluorescence. Correspondingly, MPO/ROS-pretreated TTN more significantly reduced the expression of TNF-α in LPS-stimulated macrophages than pristine TTN (Supporting Information Fig. S17). Collectively, these results substantiated that Tyr decoration can significantly increase cellular uptake as well as anti-oxidative and anti-inflammatory activities of TN.

Subsequently, *in vivo* efficacies of two nanotherapies TN and TTN were compared in mice with DSS-induced acute colitis (Fig. 7C). Consistent with the enhanced biological activities *in vitro*, TTN at 35 mg/kg more significantly inhibited the weight loss and reduction of colon length (Fig. 7D–F), as compared to TN. Likewise, the lowest levels of MPO, H_2O_2, TNF-α, and IL-1β in the colonic tissues were detected in the TTN group (Fig. 7G–J). Moreover, the colon injury was notably alleviated by TTN treatment (Fig. 7K). It is worth noting that the efficacious discrepancy of TN between this and aforementioned experiments should be owing to different batches of model animals.

Encouraged by the above results, we further examined therapeutic effects of TTN in mice with acute liver injury. First, the enhanced liver targeting capability of TTN was validated. At 16 h after i.v. injection of Cy5-TTN in mice with or without APAP-induced acute liver injury, *ex vivo* imaging showed significantly higher fluorescent signals in the isolated livers from diseased mice than those of healthy mice (Supporting Information Fig. S18). Moreover, the fluorescent intensity of Cy5-TTN was 1.9-fold higher than that of Cy5-TN in the inflammatory liver. These results demonstrated the enhanced targeting capacity of TPCD nanoparticles after Tyr decoration, largely resulting from inflammation-triggered aggregation. This finding is consistent with that based on PLGA nanoparticles. Then *in vivo* efficacies of TTN were assessed after i.v. administration at 6 h after APAP challenge in mice. TTN treatment significantly reduced the expression levels of total bilirubin (TBil), direct bilirubin (DBil), alanine aminotransferase (ALT),

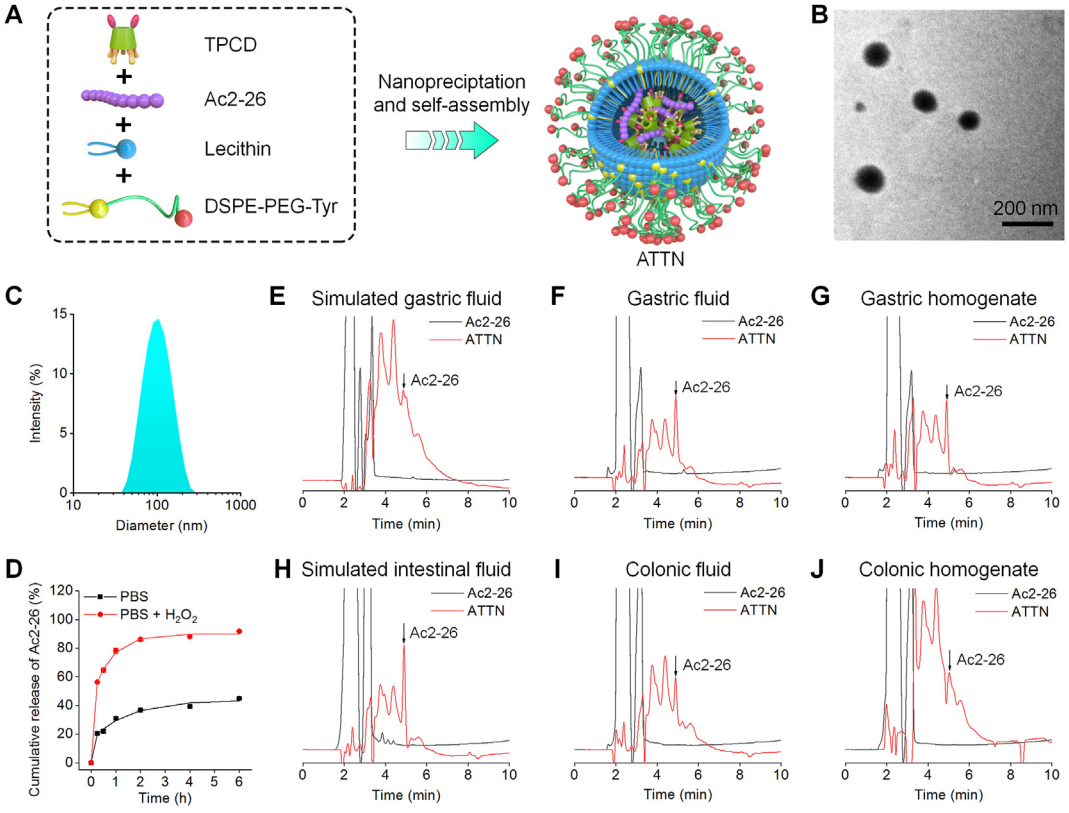

Figure 9 Engineering of a peptide Ac2-26 nanotherapy based on TTN. (A) Schematic illustration of preparation of Ac2-26-loaded TTN (*i.e.*, ATTN). (B and C) A typical TEM image (B) and size distribution (C) of ATTN. (D) *In vitro* release profiles of Ac2-26 from ATTN in PBS with or without 2.5 mmol/L H_2O_2. (E–J) Chemical stability of Ac2-26 in ATTN after incubation in different simulated gastric or intestinal fluids.

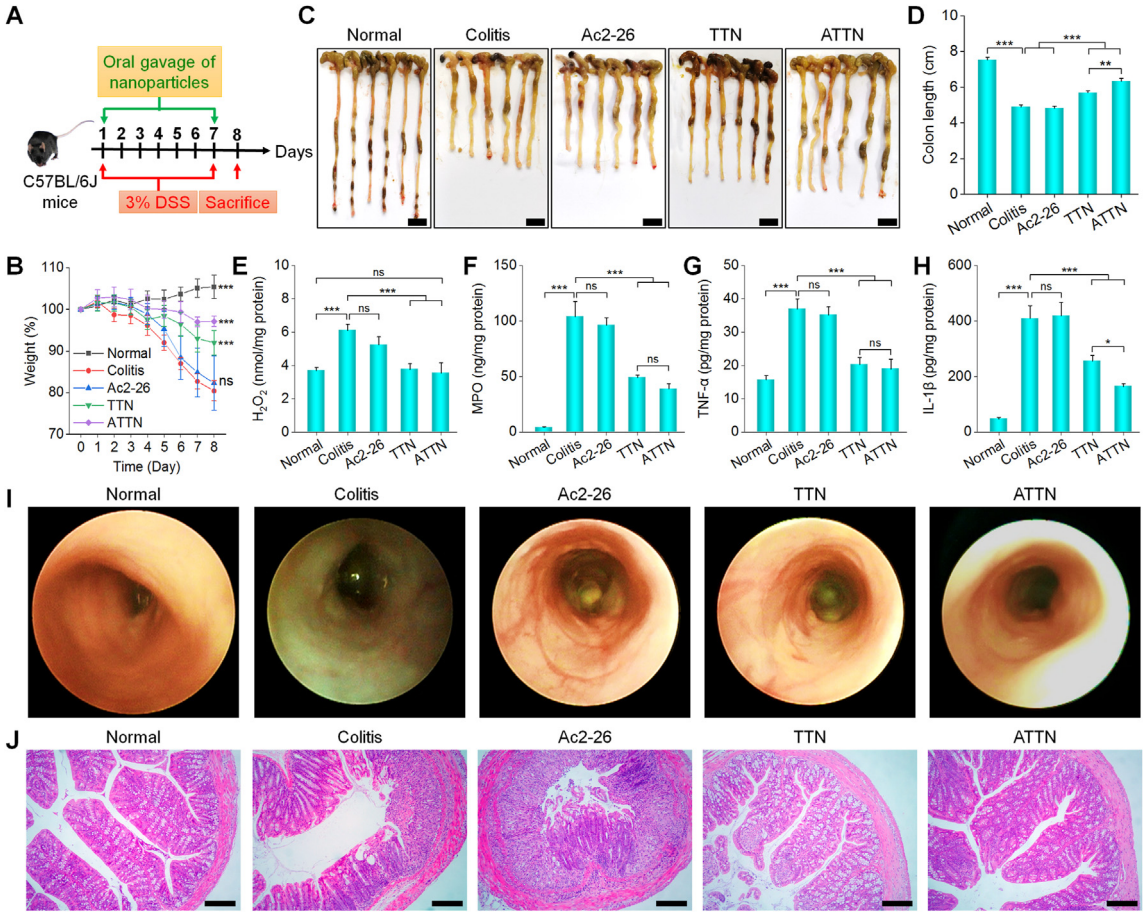

Figure 10 *In vivo* therapeutic effects of ATTN in mice with DSS-induced acute colitis. (A) Treatment regimens. (B) Changes in the body weight of mice during 7 days of treatment. $***P < 0.001$ and ns (no significance) *versus* the colitis group. (C and D) Representative digital photos (C) and quantified lengths (D) of colons isolated from mice subjected to different treatments. Scale bars, 10 mm. (E−H) The levels of H_2O_2 (E), MPO (F), TNF-α (G), and IL-1β (H) in colonic tissues. (I) Representative mini-endoscopic photos of colons from mice on Day 8 after different treatments. (J) H&E-stained histological sections of colonic tissues. Scale bars, 100 μm. All data are presented as mean ± SE (B, D, $n = 6$; E−H, $n = 5$). $*P < 0.05$, $**P < 0.01$, $***P < 0.001$; ns, no significance.

and aspartate transaminase (AST), which are typical biomarkers relevant to liver function (Fig. 8A−D). Also, notably decreased hepatic levels of H_2O_2, MPO, TNF-α, and IL-1β were detected for the TTN group, while TN showed relatively low effects (Fig. 8E−H). In addition, examination on H&E-stained liver sections revealed significant cell death and vacuolization of hepatocytes, considerable injury/necrosis of sinusoidal endothelial cells, and massive inflammatory cell infiltration in the model group (Fig. 8I), which are typical pathological changes for acute liver injury[69]. While TN treatment partly alleviated liver injury, more efficacious effects were achieved by TTN. Compared to mice in the APAP group, mice treated with TN or TTN exhibited much less hepatocellular necrosis and apoptosis as illustrated by the terminal deoxynucleotidyl transferase dUTP nick-end labeling (TUNEL) assay (Fig. 8J). Furthermore, inspection of H&E-stained histological sections of other major organs, including the heart, spleen, lung, and kidney, showed no distinguishable injuries in TTN-treated groups (Supporting Information Fig. S19), indicating good safety performance of TTN after i.v. delivery. This is consistent with the fact that TPCD can be hydrolyzed under physiological conditions and produce biocompatible compounds that will be easily excreted through the kidneys.

In line with *in vitro* cell culture studies, these *in vivo* results substantiated that peripheral functionalization with phenolic moieties can notably enhance therapeutic effects of TPCD nanoparticles for targeted therapy of diseases associated with acute inflammation and oxidative stress. The potentiated efficacy is mainly due to enhanced targeting *via* inflammation-triggered *in-situ* aggregation of phenol-coated nanoparticles.

3.7. Engineering of a pro-resolving peptide nanotherapy based on TTN for targeted treatment of colitis

According to the above encouraging findings, we reasonably hypothesize that TTN can serve as a bioactive and targeting nanoplatform for site-specific delivery of molecular therapeutics to treat inflammatory diseases. Previous studies demonstrated that a pro-resolving peptide Ac2-26 can effectively alleviate different acute and chronic inflammatory diseases, by promoting resolution of inflammation[70,71]. As a proof of concept, Ac2-26 was employed as a model drug to formulate Ac2-26-containing TTN nanoparticles (*i.e.*, ATTN), which were also prepared by the aforementioned nanoprecipitation/self-assembly method (Fig. 9A)[27]. ATTN showed well-defined spherical shape and narrow size distribution (Fig. 9B and C). *In vitro* tests showed rapid release of

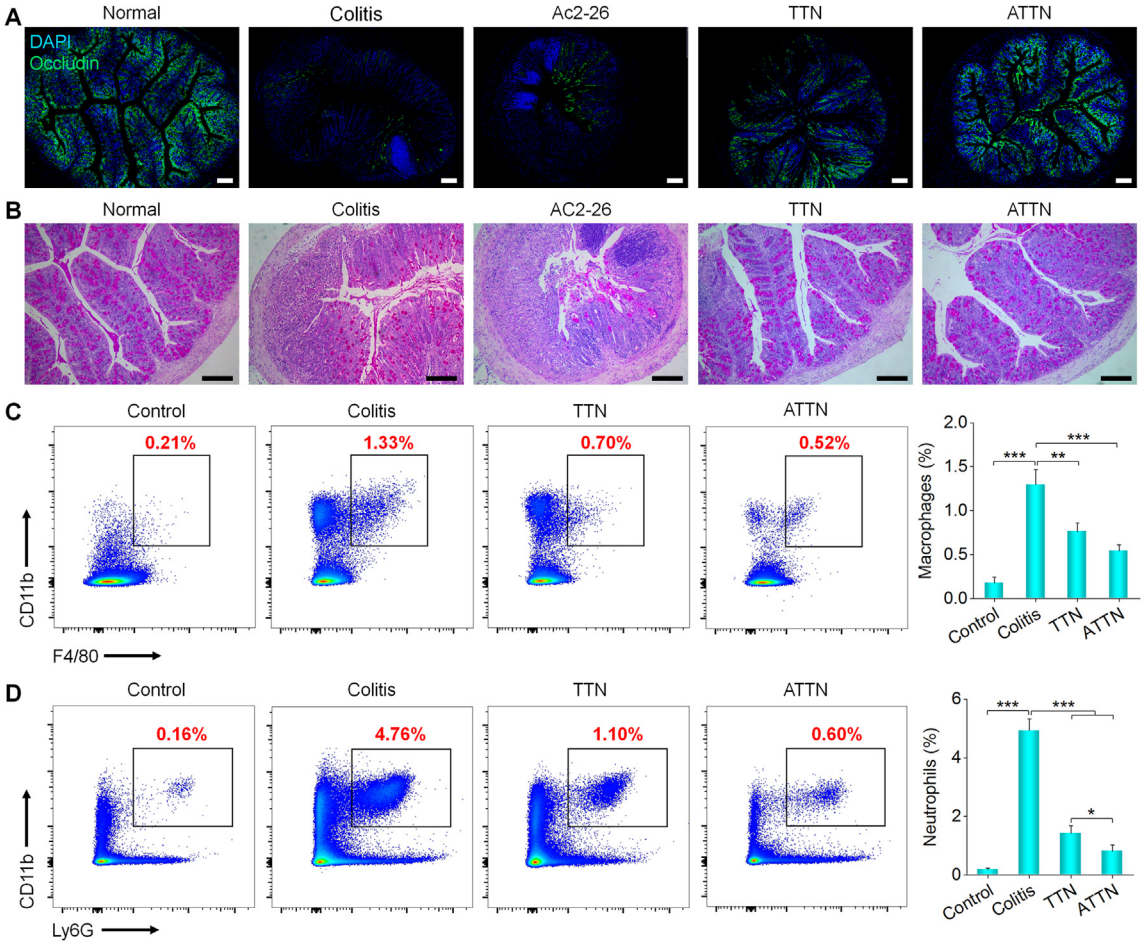

Figure 11 ATTN treatment promoted *in vivo* epithelial wound healing and attenuated infiltration of inflammatory cells. (A) Immunofluorescence analysis of the expression of occludin (green fluorescence) in colonic tissues from mice after different treatments. Scale bars, 200 μm. (B) PAS-stained histological sections of colonic tissues. Scale bars, 100 μm. (C and D) Flow cytometric analysis of $CD11b^+F4/80^+$ macrophages (C) and $CD11b^+Ly6G^+$ neutrophils (D) in colonic tissues of mice with DSS-induced acute colitis and after 7 days of different treatments. In both cases, the left panel shows representative flow cytometric profiles, while the right panel indicates quantitative results. Data in (C and D) are presented as mean ± SE ($n = 5$). $^*P < 0.05$, $^{**}P < 0.01$, $^{***}P < 0.001$.

Ac2-26 from ATTN in PBS containing H_2O_2, due to ROS-sensitive hydrolysis of TPCD (Fig. 9D)[67]. High-performance liquid chromatography (HPLC) analysis indicated that Ac2-26 encapsulated in ATTN could be clearly detected after incubation with different simulated gastric or intestinal fluids for 2 h at 37 °C, while free Ac2-26 was completely degraded in all the examined solutions (Fig. 9E–J). These results demonstrated that TTN can protect Ac2-26 from degradation or hydrolysis in harsh gastrointestinal conditions after oral administration.

Subsequently, we examined *in vitro* biological activities of ATTN in macrophages. Compared to TTN and free Ac2-26, ATTN more significantly decreased TNF-α secretion induced by LPS and more effectively suppressed ROS generation induced by PMA in macrophages (Supporting Information Fig. S20). Moreover, ATTN significantly inhibited migration of monocyte chemoattractant protein (MCP)-1-induced macrophages and activated peritoneal neutrophils (Supporting Information Fig. S21). Further, therapeutic effects of ATTN were evaluated in mice with DSS-induced acute colitis (Fig. 10A). Compared with free Ac2-26 and TTN, ATTN treatment more significantly inhibited DSS-induced weight loss and shortening of colon length (Fig. 10B–D). Also, therapy with ATTN more remarkably suppressed the expression levels of H_2O_2, MPO, TNF-α, and IL-1β in the colon tissues (Fig. 10E–H). Additionally, mini-endoscopic imaging and histopathological evaluation showed significantly less inflammation, a smaller number of ulcers, and decreased colonic mucosa damage in the ATTN group, in comparison to both Ac2-26 and TTN groups (Fig. 10I and J).

Moreover, immunofluorescence analysis was performed to examine the effect of ATTN on DSS-induced intestinal barrier dysfunction, by detecting the expression of occludin, which is a tight junction-related protein that plays an important role in gut homeostasis[72]. Compared to other controls, ATTN-treated mice showed an occludin expression pattern similar to that of normal mice (Fig. 11A). As well documented, goblet cells are mainly responsible for synthesizing and secreting mucins that form a mucosal barrier to protect epithelial cells[73]. Periodic Acid-Schiff (PAS) staining showed that ATTN treatment also more notably inhibited the depletion of goblet cells (Fig. 11B). By contrast, treatment with free Ac2-26 showed no beneficial effects. Moreover, both TTN and ATTN prevented systemic exposure of fluorescein isothiocyanate (FITC)-dextran after oral administration in colitis mice (Supporting Information Fig. S22), indicating restoration of intestinal barrier functions, in line with the results of

immunofluorescence and PAS staining. Compared with free Ac2-26 and TTN, ATTN showed the most effective wound healing efficacy. Furthermore, the counts of $CD11b^+F4/80^+$ macrophages and $CD11b^+Ly6G^+$ neutrophils recruited to the inflamed colons were dramatically reduced after 7 days of treatment with ATTN (Fig. 11C and D). Consequently, these results demonstrated that Tyr-decorated TPCD nanoparticles can function as a targeting and pharmacologically active nanovehicle for site-specifically delivering molecular therapeutics to inflammatory sites for precision and combination therapy.

3.8. *In vivo safety studies*

To highlight potential therapeutic applications of TTN, preliminary studies were performed to examine safety profiles of TTN at low (175 mg/kg) and high (350 mg/kg) doses after oral administration in mice. We found no significant weight changes and abnormal behaviors during 14 days of treatment (Supporting Information Fig. S23A). The organ indices of typical major organs showed no significant differences (Fig. S23B). Representative hematological parameters and biomarkers related to hepatic and kidney functions were in normal ranges for mice treated with TTN (Supporting Information Fig. S24). In addition, we did not find discernible injuries in H&E-stained sections of major organs and gastrointestinal tissues (Supporting Information Figs. S25 and S26). These preliminary data indicated that TTN displayed good safety performance for oral administration at doses notably higher than that used for therapeutic studies.

4. Conclusions

In summary, we successfully developed different types of phenol-functionalized nanoparticles, which can aggregate upon triggering by the inflammatory and oxidative microenvironment. Phenol-decorated nanoparticles displayed significantly enhanced accumulation in the inflammatory tissues in several mouse models of inflammatory diseases including colitis, acute liver injury, and acute lung injury, mainly resulting from *in-situ* cross-linking and assembly of nanoparticles triggered by endogenous MPO and ROS. By combining a cyclodextrin-based bioactive material with Tyr decoration, a multifunctional nanotherapy TTN was engineered, which showed significantly enhanced cellular uptake, inflammatory tissue accumulation capacity, and anti-inflammatory activities, thereby endowing notably amplified therapeutic effects in mice with colitis and acute liver injury. In addition, TTN can serve as a bioactive and inflammation-targeting nanoplatform for site-specific delivery of therapeutic agents to inflammatory sites, resulting in notably potentiated *in vivo* efficacies. Moreover, preliminary studies demonstrated a good safety profile of TTN for oral and i.v. delivery. Accordingly, phenol-decorated nanoparticles are promising targeting delivery carriers for precision therapy of inflammatory diseases. Surface molecular engineering of nanomaterials *via* phenolic moieties represents an intriguing strategy for developing inflammation-targeting delivery systems. Importantly, the underlying design principle can be generalized to amplify the targeting capacity of nanocarriers for other diseases.

Acknowledgments

This study was supported by the National Natural Science Foundation of China (No. 81971727), the Program for Postdoctoral Innovative Talent of Chongqing (China), the Program for Scientific and Technological Innovation Leader of Chongqing (No. CQYC20210302362, China), and the Program for Distinguished Young Scholars of TMMU (China).

Author contributions

Jianxiang Zhang conceptualized and designed the research. Qiang Nie, Chenwen Li, and Yu Wang carried out most of the experiments and performed data analysis. Yi Hu, Qixiong Zhang, Jiajun Cai, and Yongyao Lin participated in part of *in vitro* experiments. Gang Li, Chenping Wang, Lanlan Li, and Yin Dou participated in part of *in vivo* experiments. Wendan Pu drew the graphical abstract and sketches in all figures. Qiang Nie and Chenwen Li wrote the manuscript. Jianxiang Zhang revised the manuscript. All of the authors have read and approved the final manuscript.

Conflicts of interest

The authors have no conflicts of interest to declare.

Appendix A. Supporting information

Supporting data to this article can be found online at https://doi.org/10.1016/j.apsb.2022.07.013.

References

1. Chovatiya R, Medzhitov R. Stress, inflammation, and defense of homeostasis. *Mol Cell* 2014;**54**:281–8.
2. Nathan C. Points of control in inflammation. *Nature* 2002;**420**:846–52.
3. Weiss U. Inflammation. *Nature* 2008;**454**:427.
4. Tabas I, Glass CK. Anti-inflammatory therapy in chronic disease: challenges and opportunities. *Science* 2013;**339**:166–72.
5. Kotas ME, Medzhitov R. Homeostasis, inflammation, and disease susceptibility. *Cell* 2015;**160**:816–27.
6. Jaeschke H, Hasegawa T. Role of neutrophils in acute inflammatory liver injury. *Liver Int* 2006;**26**:912–9.
7. Woolbright BL, Jaeschke H. The impact of sterile inflammation in acute liver injury. *J Clin Transl Res* 2017;**3**:170–88.
8. Weisberg SP, McCann D, Desai M, Rosenbaum M, Leibel RL, Ferrante Jr AW. Obesity is associated with macrophage accumulation in adipose tissue. *J Clin Invest* 2003;**112**:1796–808.
9. Gurel-Gokmen B, Ipekci H, Oktay S, Alev B, Ustundag UV, Ak E, et al. Melatonin improves hyperglycemia-induced damages in rat brain. *Diabetes Metab Res Rev* 2018;**34**:e3060.
10. Polimeni L, Del Ben M, Baratta F, Perri L, Albanese F, Pastori D, et al. Oxidative stress: new insights on the association of non-alcoholic fatty liver disease and atherosclerosis. *World J Hepatol* 2015;**7**:1325–36.
11. Paravicini TM, Touyz RM. Redox signaling in hypertension. *Cardiovasc Res* 2006;**71**:247–58.
12. Fan D, Takawale A, Lee J, Kassiri Z. Cardiac fibroblasts, fibrosis and extracellular matrix remodeling in heart disease. *Fibrogenesis Tissue Repair* 2012;**5**:15.
13. Kaplan GG, Ng SC. Understanding and preventing the global increase of inflammatory bowel disease. *Gastroenterology* 2017;**152**:313–21.
14. Amor S, Puentes F, Baker D, van der Valk P. Inflammation in neurodegenerative diseases. *Immunology* 2010;**129**:154–69.
15. Barnes PJ. How corticosteroids control inflammation: quintiles prize lecture 2005. *Br J Pharmacol* 2006;**148**:245–54.
16. Vane JR, Botting RM. Mechanism of action of nonsteroidal anti-inflammatory drugs. *Am J Med* 1998;**104**:2S–8S.

17. Li P, Zheng Y, Chen X. Drugs for autoimmune inflammatory diseases: from small molecule compounds to anti-TNF biologics. *Front Pharmacol* 2017;**8**:460.
18. Gabriel SE, Jaakkimainen L, Bombardier C. Risk for serious gastrointestinal complications related to use of nonsteroidal anti-inflammatory drugs: a meta-analysis. *Ann Intern Med* 1991;**115**:787−96.
19. Buchman AL. Side effects of corticosteroid therapy. *J Clin Gastroenterol* 2001;**33**:289−94.
20. Howard PA, Delafontaine P. Nonsteroidal anti-inflammatory drugs and cardiovascular risk. *J Am Coll Cardiol* 2004;**43**:519−25.
21. Andrade RJ, Chalasani N, Björnsson ES, Suzuki A, Kullak-Ublick GA, Watkins PB, et al. Drug-induced liver injury. *Nat Rev Dis Prim* 2019;**5**:58.
22. Khilfeh I, Guyette E, Watkins J, Danielson D, Gross D, Yeung K. Adherence, persistence, and expenditures for high-cost anti-inflammatory drugs in rheumatoid arthritis: an exploratory study. *J Manag Care Spec Pharm* 2019;**25**:461−7.
23. Dinarello CA. Anti-inflammatory agents: present and future. *Cell* 2010;**140**:935−50.
24. Kotla NG, Rana S, Sivaraman G, Sunnapu O, Vemula PK, Pandit A, et al. Bioresponsive drug delivery systems in intestinal inflammation: state-of-the-art and future perspectives. *Adv Drug Deliv Rev* 2019;**146**:248−66.
25. Deng ZY, Liu SY. Inflammation-responsive delivery systems for the treatment of chronic inflammatory diseases. *Drug Deliv Transl Res* 2021;**11**:1475−97.
26. Dou Y, Li CW, Li LL, Guo JW, Zhang JX. Bioresponsive drug delivery systems for the treatment of inflammatory diseases. *J Control Release* 2020;**327**:641−66.
27. Li CW, Zhao Y, Cheng J, Guo JW, Zhang QX, Zhang XJ, et al. A proresolving peptide nanotherapy for site-specific treatment of inflammatory bowel disease by regulating proinflammatory microenvironment and gut microbiota. *Adv Sci* 2019;**6**:1900610.
28. Zhang QX, Tao H, Lin YY, Hu Y, An HJ, Zhang DL, et al. A superoxide dismutase/catalase mimetic nanomedicine for targeted therapy of inflammatory bowel disease. *Biomaterials* 2016;**105**:206−21.
29. Li CW, Dou Y, Chen YD, Qi YT, Li LL, Han SL, et al. Site-specific microRNA-33 antagonism by pH-responsive nanotherapies for treatment of atherosclerosis *via* regulating cholesterol efflux and adaptive immunity. *Adv Funct Mater* 2020;**30**:2002131.
30. Dou Y, Chen Y, Zhang XJ, Xu XQ, Chen YD, Guo JW, et al. Non-proinflammatory and responsive nanoplatforms for targeted treatment of atherosclerosis. *Biomaterials* 2017;**143**:93−108.
31. Yang GY, Song JL, Zhang JX. Biomimetic and bioresponsive nanotherapies for inflammatory vascular diseases. *Nanomedicine (Lond)* 2020;**15**:1917−21.
32. Ramelli SC, Comer BS, McLendon JM, Sandy LL, Ferretti AP, Barrington R, et al. Nanoparticle delivery of anti-inflammatory LNA oligonucleotides prevents airway inflammation in a HDM model of asthma. *Mol Ther Nucleic Acids* 2020;**19**:1000−14.
33. da Silva AL, de Oliveira GP, Kim N, Cruz FF, Kitoko JZ, Blanco NG, et al. Nanoparticle-based thymulin gene therapy therapeutically reverses key pathology of experimental allergic asthma. *Sci Adv* 2020;**6**:eaay7973.
34. Niu XQ, Chen JJ, Gao JQ. Nanocarriers as a powerful vehicle to overcome blood-brain barrier in treating neurodegenerative diseases: focus on recent advances. *Asian J Pharm Sci* 2019;**14**:480−96.
35. Verma S, Utreja P. Vesicular nanocarrier-based treatment of skin fungal infections: potential and emerging trends in nanoscale pharmacotherapy. *Asian J Pharm Sci* 2019;**14**:117−29.
36. Li CW, Li LL, Chen S, Zhang JX, Lu WL. Antioxidant nanotherapies for the treatment of inflammatory diseases. *Front Bioeng Biotechnol* 2020;**8**:200.
37. Li CW, Wu PD, Dou Y, Li Q, Zhang JX. Bioresponsive nanoplatforms for imaging and therapy of cardiovascular diseases. *View* 2022;**3**:20200137.
38. Wu Y, Zhang Y, Dai LL, Wang QQ, Xue LJ, Su ZG, et al. An apoptotic body-biomimic liposome *in situ* upregulates anti-inflammatory macrophages for stabilization of atherosclerotic plaques. *J Control Release* 2019;**316**:236−49.
39. Chung BL, Toth MJ, Kamaly N, Sei YJ, Becraft J, Mulder WJ, et al. Nanomedicines for endothelial disorders. *Nano Today* 2015;**10**:759−76.
40. Flores AM, Hosseini-Nassab N, Jarr KU, Ye JQ, Zhu XJ, Wirka R, et al. Pro-efferocytic nanoparticles are specifically taken up by lesional macrophages and prevent atherosclerosis. *Nat Nanotechnol* 2020;**15**:154−61.
41. He W, Kapate N, Shields CW, Mitragotri S. Drug delivery to macrophages: a review of targeting drugs and drug carriers to macrophages for inflammatory diseases. *Adv Drug Deliv Rev* 2020;**165−166**:15−40.
42. Brusini R, Varna M, Couvreur P. Advanced nanomedicines for the treatment of inflammatory diseases. *Adv Drug Deliv Rev* 2020;**157**:161−78.
43. Zhang DL, Zhang JX. Surface engineering of nanomaterials with phospholipid-polyethylene glycol-derived functional conjugates for molecular imaging and targeted therapy. *Biomaterials* 2020;**230**:119646.
44. Jin K, Luo ZM, Zhang B, Pang ZQ. Biomimetic nanoparticles for inflammation targeting. *Acta Pharm Sin B* 2018;**8**:23−33.
45. Yan HZ, Shao D, Lao Y-H, Li MQ, Hu HZ, Leong KW. Engineering cell membrane-based nanotherapeutics to target inflammation. *Adv Sci* 2019;**6**:1900605.
46. Yang GY, Chen S, Zhang JX. Bioinspired and biomimetic nanotherapies for the treatment of infectious diseases. *Front Pharmacol* 2019;**10**:751.
47. Park JH, Dehaini D, Zhou JR, Holay M, Fang RH, Zhang LF. Biomimetic nanoparticle technology for cardiovascular disease detection and treatment. *Nanoscale Horiz* 2020;**5**:25−42.
48. Cheng J, Zhang RJ, Li CW, Tao H, Dou Y, Wang YQ, et al. A targeting nanotherapy for abdominal aortic aneurysms. *J Am Coll Cardiol* 2018;**72**:2591−605.
49. Molinaro R, Corbo C, Martinez JO, Taraballi F, Evangelopoulos M, Minardi S, et al. Biomimetic proteolipid vesicles for targeting inflamed tissues. *Nat Mater* 2016;**15**:1037−46.
50. Gao C, Huang QX, Liu CH, Kwong CHT, Yue LD, Wan JB, et al. Treatment of atherosclerosis by macrophage-biomimetic nanoparticles *via* targeted pharmacotherapy and sequestration of proinflammatory cytokines. *Nat Commun* 2020;**11**:2622.
51. Hu XL, Yang GY, Chen S, Luo SX, Zhang JX. Biomimetic and bioinspired strategies for oral drug delivery. *Biomater Sci* 2020;**8**:1020−44.
52. Zhang XJ, Xu XQ, Chen YD, Dou Y, Zhou X, Li LL, et al. Bioinspired yeast microcapsules loaded with self-assembled nanotherapies for targeted treatment of cardiovascular disease. *Mater Today* 2017;**20**:301−13.
53. Zhao ZM, Pan DC, Qi QM, Kim J, Kapate N, Sun T, et al. Engineering of living cells with polyphenol-functionalized biologically active nanocomplexes. *Adv Mater* 2020;**32**:e2003492.
54. Zhou X, Zhang XJ, Han SL, Dou Y, Liu MY, Zhang L, et al. Yeast microcapsule-mediated targeted delivery of diverse nanoparticles for imaging and therapy *via* the oral route. *Nano Lett* 2017;**17**:1056−64.
55. Lu Y, Aimetti AA, Langer R, Gu Z. Bioresponsive materials. *Nat Rev Mater* 2016;**2**:16075.
56. Michon T, Chenu M, Kellershon N, Desmadril M, Guéguen J. Horseradish peroxidase oxidation of tyrosine-containing peptides and their subsequent polymerization: a kinetic study. *Biochemistry* 1997;**36**:8504−13.
57. Lee J, Ju M, Cho OH, Kim Y, Nam KT. Tyrosine-rich peptides as a platform for assembly and material synthesis. *Adv Sci* 2018;**6**:1801255.
58. Bogdanov A, Matuszewski L, Bremer C, Petrovsky A, Weissleder R. Oligomerization of paramagnetic substrates result in signal amplification and can be used for MR imaging of molecular targets. *Mol Imag* 2002;**1**:16−23.

59. Chen JW, Pham W, Weissleder R, Bogdanov Jr A. Human myeloperoxidase: a potential target for molecular MR imaging in atherosclerosis. *Magn Reson Med* 2004;**52**:1021−8.
60. Querol M, Chen JW, Weissleder R, Bogdanov Jr A. DTPA-bisamide-based MR sensor agents for peroxidase imaging. *Org Lett* 2005;**7**:1719−22.
61. Wadghiri YZ, Hoang DM, Leporati A, Gounis MJ, Rodríguez-Rodríguez A, Mazzanti ML, et al. High-resolution imaging of myeloperoxidase activity sensors in human cerebrovascular disease. *Sci Rep* 2018;**8**:7687.
62. Tao H, Guo JW, Ma YC, Zhao Y, Jin TT, Gu LJ, et al. Luminescence imaging of acute liver injury by biodegradable and biocompatible nanoprobes. *ACS Nano* 2020;**14**:11083−99.
63. Xu XQ, An HJ, Zhang DL, Tao H, Dou Y, Li XH, et al. A self-illuminating nanoparticle for inflammation imaging and cancer therapy. *Sci Adv* 2019;**5**:eaat2953.
64. Guo JW, Tao H, Dou Y, Li LL, Xu XQ, Zhang QX, et al. A myeloperoxidase-responsive and biodegradable luminescent material for real-time imaging of inflammatory diseases. *Mater Today* 2017;**20**:493−500.
65. Rodriguez E, Nilges M, Weissleder R, Chen JW. Activatable magnetic resonance imaging agents for myeloperoxidase sensing: mechanism of activation, stability, and toxicity. *J Am Chem Soc* 2010;**132**:168−77.
66. Dhayal SK, Sforza S, Wierenga PA, Gruppen H. Peroxidase induced oligo-tyrosine cross-links during polymerization of α-lactalbumin. *Biochim Biophys Acta* 2015;**1854**:1898−905.
67. Li LL, Guo JW, Wang YQ, Xiong XX, Tao H, Li J, et al. A broad-spectrum ROS-eliminating material for prevention of inflammation and drug-induced organ toxicity. *Adv Sci* 2018;**5**:1800781.
68. Chow CW, Herrera Abreu MT, Suzuki T, Downey GP. Oxidative stress and acute lung injury. *Am J Respir Cell Mol Biol* 2003;**29**:427−31.
69. Marques PE, Amaral SS, Pires DA, Nogueira LL, Soriani FM, Lima BH, et al. Chemokines and mitochondrial products activate neutrophils to amplify organ injury during mouse acute liver failure. *Hepatology* 2012;**56**:1971−82.
70. Fredman G, Kamaly N, Spolitu S, Milton J, Ghorpade D, Chiasson R, et al. Targeted nanoparticles containing the proresolving peptide Ac2-26 protect against advanced atherosclerosis in hypercholesterolemic mice. *Sci Transl Med* 2015;**7**:275ra20.
71. Kamaly N, Fredman G, Subramanian M, Gadde S, Pesic A, Cheung L, et al. Development and *in vivo* efficacy of targeted polymeric inflammation-resolving nanoparticles. *Proc Natl Acad Sci U S A* 2013;**110**:6506−11.
72. Citi S. Intestinal barriers protect against disease. *Science* 2018;**359**:1097−8.
73. Kim JJ, Khan WI. Goblet cells and mucins: role in innate defense in enteric infections. *Pathogens* 2013;**2**:55−70.